J. Fluid Mech. (1998), *vol.* 367, *pp.* 163–203. Printed in the United Kingdom

Droplet–turbulence interactions in low-Mach-number homogeneous shear two-phase flows

By FARZAD MASHAYEK

Department of Mechanical Engineering, University of Hawaii at Manoa, 2540 Dole Street, Honolulu, HI 96822, USA

(Received 25 October 1996 and in revised form 3 February 1998)

Several important issues pertaining to dispersion and polydispersity of droplets in turbulent flows are investigated via direct numerical simulation (DNS). The carrier phase is considered in the Eulerian context, the dispersed phase is tracked in the Lagrangian frame and the interactions between the phases are taken into account in a realistic two-way (coupled) formulation. The resulting scheme is applied for extensive DNS of low-Mach-number, homogeneous shear turbulent flows laden with droplets. Several cases with one- and two-way couplings are considered for both non-evaporating and evaporating droplets. The effects of the mass loading ratio, the droplet time constant, and thermodynamic parameters, such as the droplet specific heat, the droplet latent heat of evaporation, and the boiling temperature, on the turbulence and the droplets are investigated. The effects of the initial droplet temperature and the initial vapour mass fraction in the carrier phase are also studied. The gravity effects are not considered as the numerical methodology is only applicable in the absence of gravity. The evolution of the turbulence kinetic energy and the mean internal energy of both phases is studied by analysing various terms in their transport equations. The results for the non-evaporating droplets show that the presence of the droplets decreases the turbulence kinetic energy of the carrier phase while increasing the level of anisotropy of the flow. The droplet streamwise velocity variance is larger than that of the fluid, and the ratio of the two increases with the increase of the droplet time constant. Evaporation increases both the turbulence kinetic energy and the mean internal energy of the carrier phase by mass transfer. In general, evaporation is controlled by the vapour mass fraction gradient around the droplet when the initial temperature difference between the phases is negligible. In cases with small initial droplet temperature, on the other hand, the convective heat transfer is more important in the evaporation process. At long times, the evaporation rate approaches asymptotic values depending on the values of various parameters. It is shown that the evaporation rate is larger for droplets residing in high-strain-rate regions of the flow, mainly due to larger droplet Reynolds numbers in these regions. For both the evaporating and the non-evaporating droplets, the root mean square (r.m.s.) of the temperature fluctuations of both phases becomes independent of the initial droplet temperature at long times. Some issues relevant to modelling of turbulent flows laden with droplets are also discussed.

1. Introduction

A complex issue in the theoretical description of turbulent flows is the phenomena of 'dispersion' and 'polydispersity' of liquid droplets (Faeth 1983, 1987; Williams 1985). With the presence of such droplets in a carrier turbulent fluid, the additional physical complexities due to multiphase transport including the couplings between the various phases, make the mathematical description of the problem very complex. Due to its physical nature, the mechanism of dispersion is best understood when analysed in the Lagrangian context (Taylor 1921; Corrsin 1961). This alone makes investigation via numerical simulations very convenient.

The implementation of direct numerical simulation (DNS) in two-phase flows to investigate the dispersion of particles in decaying isotropic turbulence was pioneered by Riley & Patterson (1974). Using a low-resolution simulation (32^3 grid points) and a relatively small number of particles (432), they found that an increase of the particle inertia increases the velocity autocorrelation. McLaughlin (1989) simulated particle deposition in a channel flow and showed the tendency of particles to accumulate in the viscous sublayer. Squires & Eaton (1990, 1991*a*, *b*) simulated both stationary and decaying turbulence fields with one- and two-way coupling. The results show the increase of the eddy diffusivity of heavy particles over that of the fluid particle for cases with one-way coupling. In the cases with two-way coupling they found that the fraction of energy at high wavenumbers of the spatial energy spectrum of turbulence increases relative to that at low wavenumbers as the mass loading ratio is increased. They also found that large particles tend to collect preferentially in regions of low vorticity and high strain. Later, Squires & Eaton (1994) used the data generated by these simulations to investigate some issues relevant to turbulence modifications by particles. They examined the values used for the empirical constants appearing in the transport equation for the dissipation rate of the fluid turbulence kinetic energy. Elghobashi & Truesdell (1992, 1993); Truesdell & Elghobashi (1994) conducted similar studies. They considered the full equation for the particle motion and showed that for large density ratios the Stokes drag is of primary importance. In the presence of both gravity and two-way coupling they showed that energy is transferred from the gravity direction to other directions by the pressure–strain correlation.

The settling velocity of heavy particles in isotropic turbulence was studied by Wang & Maxey (1993) for different particle time constants and drift velocities. The results show an increase of the settling velocity for all cases. The maximum increase in settling velocity is obtained when both the particle time constant and the drift velocity are comparable to the Kolmogorov scales. Samimy & Lele (1991) studied the motion of heavy particles in a compressible free shear flow using a compact finite difference scheme. They concluded that, for the range of convective Mach numbers between 0.2 and 0.6, compressibility does not significantly affect the motion of the particles. Mashayek *et al.* (1997*a*) studied dispersion and polydispersity of evaporating droplets in incompressible, stationary, isotropic turbulent flows. Later, Mashayek (1998) relaxed the one-way coupling assumption invoked in Mashayek *et al.* (1997*a*) and investigated dispersion of evaporating droplets in a compressible carrier phase. These studies have been very instructive in exhibiting many important features of dispersion and polydispersity in 'isotropic' flows. In the present study, we consider a homogeneous shear configuration which is very convenient for investigating the anisotropy effects.

In order to fully consider a two-way coupling between the evaporating droplets and the carrier phase, it is necessary to account for density variations in the carrier phase.

This is accomplished by considering the compressible flow, although a study of high-compressibility effects is not intended. The literature is very rich in both theoretical and computational studies of (single-phase) compressible flows. An extensive review of the previous works is not included; we refer to Blaisdell, Mansour & Reynolds (1993) for a recent review. Here, we are more concerned with the computational methodologies implemented for direct numerical simulations of compressible flows. It appears that high-order finite difference (e.g. Lee, Lele & Moin 1991) and spectral collocation methods are more popular than other schemes. Although spectral methods are more accurate and simple, they have difficulties in capturing sharp discontinuities (such as shocklets) in the solution domain. To overcome this shortcoming, one has either to use a very high-resolution grid (in the order of eight grid points per discontinuity (Passot & Pouquet 1987), or to consider only low Mach numbers such that the flow remains free of shocklets. The most common set of equations considered for compressible flows involve the conservation equations for mass, momentum, and total energy (Kida & Orszag 1990, 1992; Blaisdell *et al.* 1993; Miura & Kida 1995). Alternatively, an equation may be considered for the pressure instead of the total energy equation (Sarkar, Erlebacher & Hussaini 1991, 1992; Sarkar 1994). The choice of the fourth (the total energy or the pressure) equation depends on the problem under investigation.

The objective of this work is to perform an extensive DNS study of the dispersion and polydispersity of droplets in low-Mach-number homogeneous shear turbulent flows. The specific objectives are: (i) to develop a realistic formulation (suitable for DNS) that accounts for interactions between the two phases, (ii) to identify and to investigate the effects of the parameters that influence the fate of the droplets and the flow, (iii) to make use of the DNS results to identify various mechanisms by which the two phases most effectively interact, (iv) to enhance our understanding of the evaporation phenomena in two-phase turbulent flows, and (v) to perform a comparative assessment of the effects of evaporation on the statistics of the flow and the droplets via comparisons between the results of the cases with evaporating and non-evaporating droplets. Furthermore, some issues of relevance to modelling of two-phase flows are considered. It must be emphasized here that due to the complexity of the problem, the number of parameters influencing the two-phase flow is large. Since there is no previous study of evaporating droplets interacting with a compressible flow, it is not clear which group of parameters are more important than the others. In fact, the level of importance of a particular parameter may depend on the physical phenomenon under consideration. Therefore, the present study considers a large number of parameters with limited ranges of variation rather than focusing on one or two parameter(s) with wide range(s) of variation. The results of this study can be used to efficiently (design and) conduct more focused future investigations on this subject. In § 2 the problem formulation is provided followed by a description of the computational methodology in § 3. The results of the simulations of the non-evaporating and evaporating droplets are presented and discussed in §§ 4 and 5, respectively. A summary of this study is furnished in § 6, along with some concluding remarks.

2. Problem formulation

This work deals with DNS of homogeneous turbulent shear flow of a compressible gas laden with droplets. The governing equations considered here are the compressible forms of the continuity, momentum, and energy equations for the continuous phase

coupled with the Lagrangian equations for discrete droplets. Also, a conservation equation (in the Eulerian frame) is considered for the vapour mass fraction. For simplicity, the vapour is assumed to have the same molecular weight, viscosity, mass diffusivity, and specific heat as those of the gas. In this manner, the gas–vapour mixture (hereinafter also referred to as the carrier phase or the fluid) is treated as one entity – the continuity, momentum, and energy equations are solved for the gas–vapour mixture. The specific enthalpy of the vapour, however, is considered to be different than that of the gas in order to satisfy the first law of thermodynamics. In the following, we present the equations for the continuous and the dispersed phases along with a discussion of the numerical treatment of these equations in a homogeneous shear configuration.

2.1. *Gas–vapour equations*

The carrier phase (composed of the gas and the vapour) is considered to be a compressible and Newtonian fluid with zero bulk viscosity, and to obey the perfect gas equation of state. The instantaneous density, velocity, pressure, and temperature of the carrier phase are denoted by ρ, U_i, P, and T, respectively. The instantaneous vapour mass fraction is denoted by Y. With this nomenclature, the Eulerian forms of the non-dimensional continuity, momentum, and energy equations for the carrier phase are given by

$$\frac{\partial \rho}{\partial t} + \frac{\partial}{\partial x_j}(\rho U_j) = \mathscr{S}_m, \tag{1}$$

$$\frac{\partial}{\partial t}(\rho U_i) + \frac{\partial}{\partial x_j}(\rho U_i U_j) = -\frac{\partial P}{\partial x_i} + \frac{2}{Re_f}\frac{\partial}{\partial x_j}\left(S_{ij} - \tfrac{1}{3}\Delta\delta_{ij}\right) + \mathscr{S}_{ui}, \tag{2}$$

$$\frac{\partial E_T}{\partial t} + \frac{\partial}{\partial x_j}\left[U_j(E_T + P)\right] = \frac{1}{(\gamma - 1)Re_f Pr M_f^2}\frac{\partial^2 T}{\partial x_j \partial x_j} + \frac{2}{Re_f}\frac{\partial}{\partial x_j}\left[U_i\left(S_{ij} - \tfrac{1}{3}\Delta\delta_{ij}\right)\right] + \mathscr{S}_e, \tag{3}$$

and the conservation equation for the vapour mass fraction is described as

$$\frac{\partial}{\partial t}(\rho Y) + \frac{\partial}{\partial x_j}(\rho Y U_j) = \frac{1}{Re_f Sc}\frac{\partial^2 Y}{\partial x_j \partial x_j} + \mathscr{S}_m. \tag{4}$$

The total energy (E_T) is the summation of the sensible internal energy ($\rho C_v T$, where C_v is the specific heat of the carrier phase) and the kinetic energy ($\frac{1}{2}\rho U_i U_i$) of the gas–vapour mixture. The equation of state is $P = \rho T/\gamma M_f^2$. In the above equations, $\Delta = U_{j,j}$ is the dilatation ($U_{i,j} = \partial U_i/\partial x_j$), $S_{ij} = \frac{1}{2}(U_{i,j} + U_{j,i})$ is the rate-of-strain tensor, and δ_{ij} is the Kroenecker delta function. All of the variables are normalized by reference length (L_f), density (ρ_f), velocity (U_f), and temperature (T_f) scales. The reference Reynolds and Mach numbers are $Re_f = \rho_f U_f L_f/\mu$ and $M_f = U_f/(\gamma R T_f)^{1/2}$, respectively, and the Prandtl and Schmidt numbers are given by $Pr = C_p\mu/\kappa$ and $Sc = \mu/\rho\Gamma$, respectively. In these definitions, the carrier-phase variables μ, κ, C_p, γ, and R are the viscosity, the thermal conductivity, the specific heat, the ratio of the specific heats, and the gas constant, respectively, and Γ is the binary mass diffusivity coefficient. The specific enthalpies for the gas and the liquid are described as $h_g = T$ and $h_\ell = \sigma T$, respectively, where $\sigma = C_\ell/C_p$ with C_ℓ denoting the specific heat of the liquid. For evaporating droplets we only consider the case with $\sigma = 1$ for which

the specific enthalpy of the vapour is expressed as $h_v = T + \lambda$ with $\lambda = L_v/C_pT_f$ and L_v representing the latent heat of evaporation. All the enthalpies are normalized by C_pT_f. The total energy equation (3) is derived by assuming unity Lewis number ($Le \equiv Sc/Pr = 1$). The coupling of the carrier phase with the droplets is through the terms $\mathscr{S}_m$, $\mathscr{S}_{ui}$, and $\mathscr{S}_e$ which describe the mass, momentum, and energy exchange between the phases, respectively. The formulation of these terms and their calculation from the discrete droplet fields are described in § 2.4.

2.2. *Droplet equations*

The droplets are allowed to evaporate and are assumed to remain spherical with diameter smaller than the smallest length scale of the turbulence and to exhibit an empirically corrected Stokesian drag force. Both interior motions and rotation of the droplets are neglected. The density of the droplets is considered to be constant and much larger than the density of the carrier phase such that only the inertia, the drag, and the gravity forces are significant for the droplet dynamics. As will be discussed in § 2.3, the numerical methodology used in this study to simulate the homogeneous shear particle-laden flow is only applicable in the absence of gravity; therefore, buoyancy effects are not considered. In addition, the droplet volume fraction is assumed to be relatively small and both droplet–droplet interactions and heat transfer due to radiation are neglected. The droplets are tracked individually in a Lagrangian manner, and the instantaneous droplet position, velocity, temperature, and mass are given by X_i, V_i, T_d and m_d, respectively. With this nomenclature, the non-dimensional Lagrangian equations describing the droplet dynamics are (Crowe, Sharma & Stock 1977)

$$\frac{\mathrm{d}X_i}{\mathrm{d}t} = V_i, \tag{5}$$

$$\frac{\mathrm{d}V_i}{\mathrm{d}t} = \frac{f_1}{\tau_d}(U_i^* - V_i), \tag{6}$$

$$\frac{\mathrm{d}T_d}{\mathrm{d}t} = \frac{f_2}{\tau_d}(T^* - T_d) - \frac{f_3}{\tau_d}(Y_s - Y^*), \tag{7}$$

and

$$\frac{\mathrm{d}m_d}{\mathrm{d}t} = -f_4\tau_d^{1/2}(Y_s - Y^*), \tag{8}$$

where the superscript * indicates the value of a carrier-phase variable at the droplet location, and Y_s is the vapour mass fraction at the surface of the droplet.

The non-dimensional droplet time constant, based on the Stokesian drag of a sphere, is

$$\tau_d = \frac{Re_f\rho_d d_d^2}{18}, \tag{9}$$

where d_d and ρ_d are the droplet diameter and density, respectively. The droplet variables are normalized using the same reference scales as those used for the carrier-phase variables. The function f_1 in (6) represents an empirical correction to the Stokes drag due to droplet Reynolds numbers of order unity and larger (Wallis 1969) and is valid for droplet Reynolds numbers $Re_d \leqslant 1000$ ($Re_d = Re_f\rho^* d_d|U_i^* - V_i|$):

$$f_1 = \frac{1 + 0.15Re_d^{0.687}}{1 + B}, \tag{10}$$

where $B = (T^* - T_d)/\lambda$ is the transfer number. It is noted that B is a modification due to evaporation, therefore for non-evaporating droplets $B \equiv 0$.

The droplets are assumed 'lumped', so that there is no temperature variation within each droplet. The first term on the right-hand side of (7) represents the rate of change of the droplet temperature due to convective heat transfer with the carrier phase. The factor f_2 represents a correlation for the convective heat transfer coefficient based on an empirically corrected Nusselt number ($Nu = (2 + 0.6Re_d^{0.5}Pr^{0.33})/(1 + B)$) (Bird, Stewart & Lightfoot 1960):

$$f_2 = \frac{Nu}{3Pr\sigma}. \tag{11}$$

The second term on the right-hand side of (7) represents the change in the droplet internal energy due to phase change. The correlation f_3 is a function of an empirically corrected Sherwood number ($Sh = 2 + 0.6Re_d^{0.5}Sc^{0.33}$) and is given by (Bird *et al.* 1960)

$$f_3 = \frac{\rho^* Sh}{3Sc}\frac{\lambda}{\sigma}. \tag{12}$$

The vapour mass fraction at the surface of the droplet is equal to the vaporization pressure (P_{vap}) of the droplet (for equivalent molecular weights of the gas and the liquid) and obeys the Clausius–Clapeyron equation

$$Y_s = P_{vap} = \exp\left[\frac{\gamma\lambda}{(\gamma - 1)T_B}\left(1 - \frac{T_B}{T_d}\right)\right], \tag{13}$$

where the boiling temperature of the liquid (T_B) is assumed to be independent of the pressure (i.e. constant). Finally, (8) governs the rate of mass transfer from the droplet due to evaporation which is a function of the vapour mass fraction difference at the droplet surface, the droplet time constant, and the Sherwood-number-dependent correlation:

$$f_4 = \pi\left(\frac{18}{\rho_d}\right)^{0.5}\frac{\rho^* Sh}{Re_f^{1.5}Sc}. \tag{14}$$

2.3. *Formulation for homogeneous shear configuration*

To configure a homogeneous shear flow suitable for DNS, a linear mean velocity profile is applied to a zero mean turbulent velocity field. Therefore, the carrier-phase instantaneous velocity is expressed as $U_i = Sx_2\delta_{i1} + u_i$, where u_i is the carrier-phase fluctuating velocity. The magnitude of the imposed shear is given by the amplitude of the mean velocity gradient, $S = \partial\langle U_1\rangle/\partial x_2 = \text{const.}$, where $\langle\,\rangle$ indicates the Eulerian ensemble average over the number of grid points. For homogeneous flows which either start from isotropic initial conditions or develop to become independent of the initial conditions, Blaisdell, Mansour & Reynolds (1991) show that the Favre-average fluctuating quantity is the same as the Reynolds average one. In this study we indicate the fluctuating quantity with the same notation for both types of averaging; the type of averaging is understood from the context. The primary effect of the mean shear is to provide a natural (albeit idealistic) homogeneous forcing. No stationary state is achieved, and the Reynolds number grows until the turbulence structures outgrow the box size, at which time the simulation is stopped.

In order to employ the Fourier spectral method, periodic boundary conditions must be imposed. This is accomplished by solving the governing equations for fluctuating velocities on a grid which deforms with the mean flow. This transformation has been discussed in detail by Rogallo (1981) and Blaisdell *et al.* (1991) and is only

summarized here. A computational (deforming) coordinate system (x_i') is related to the fixed (non-deforming) system through $x_i' = Q_{ij}x_j$ where the transformation tensor is defined as

$$Q_{ij} = \begin{pmatrix} 1 & -St & 0 \\ 0 & 1 & 0 \\ 0 & 0 & 1 \end{pmatrix}, \tag{15}$$

for the present conditions. Performing the transformation on (1)–(4) and dropping the superscript $'$ on the coordinates, the governing equations in the transformed coordinates are

$$\frac{\partial \rho}{\partial t} + Q_{ji}\frac{\partial}{\partial x_j}(\rho u_i) = \mathscr{S}_m, \tag{16}$$

$$\frac{\partial}{\partial t}(\rho u_i) + Q_{kj}\frac{\partial}{\partial x_k}(\rho u_i u_j) = -\rho u_2 S\delta_{i1} - Q_{ki}\frac{\partial P}{\partial x_k} + \frac{Q_{kj}}{Re_f}\frac{\partial}{\partial x_k}\left(Q_{ki}\frac{\partial u_j}{\partial x_k} + Q_{kj}\frac{\partial u_i}{\partial x_k} - \tfrac{2}{3}\Delta\delta_{ij}\right) + \mathscr{S}_{ui}, \tag{17}$$

$$\frac{\partial e_T}{\partial t} + Q_{kj}\frac{\partial}{\partial x_k}[u_j(P + e_T)] = -\rho u_1 u_2 S + \frac{S}{Re_f}\left(Q_{k2}\frac{\partial u_1}{\partial x_k} + Q_{k1}\frac{\partial u_2}{\partial x_k} + S\right) + \frac{Q_{ki}}{Re_f}\frac{\partial}{\partial x_k}\left[u_j\left(Q_{ki}\frac{\partial u_j}{\partial x_k} + Q_{kj}\frac{\partial u_i}{\partial x_k} - \tfrac{2}{3}\Delta\delta_{ij} + S\delta_{i1}\delta_{j2} + S\delta_{i2}\delta_{j1}\right)\right] + \frac{Q_{ki}Q_{ji}}{(\gamma-1)Re_f PrM_f^2}\frac{\partial^2 T}{\partial x_k \partial x_j} + \mathscr{S}_e, \tag{18}$$

$$\frac{\partial}{\partial t}(\rho Y) + Q_{kj}\frac{\partial}{\partial x_k}(\rho u_j Y) = \frac{Q_{ki}Q_{ji}}{Re_f Sc}\frac{\partial^2 Y}{\partial x_k \partial x_j} + \mathscr{S}_m, \tag{19}$$

where $\Delta = Q_{ji}u_{i,j}$, and $e_T = \rho C_v T + \frac{1}{2}\rho u_i u_i$.

In the absence of gravity or other external body forces and by assuming that the droplets start from the same initial velocities as those of their surrounding fluid elements, the droplet instantaneous velocity is described as (Simonin, Deutsch & Boivin 1995) $V_i = Sx_2\delta_{i1} + v_i$, with v_i denoting the droplet fluctuating velocity. By performing ensemble averaging on the droplet instantaneous equations, it can be shown that the dispersed phase is homogeneous within the deforming domain used to simulate the carrier phase; thus, periodic boundary conditions can be applied to the dispersed phase as well. The droplet position and momentum equations in the transformed coordinates read

$$\frac{\mathrm{d}X_i}{\mathrm{d}t} = Q_{ik}v_k, \tag{20}$$

$$\frac{\mathrm{d}v_i}{\mathrm{d}t} = \frac{f_1}{\tau_d}(u_i^* - v_i) - v_2 S\delta_{i1}. \tag{21}$$

The equations for the scalar quantities T_d and m_d remain the same as those given by (7) and (8).

2.4. *Coupling terms*

The source/sink terms $\mathscr{S}_m$, $\mathscr{S}_{ui}$, and $\mathscr{S}_e$ appearing in (16)–(19) represent the integrated effects of the droplet mass, momentum, and energy exchange with the carrier phase. These Eulerian variables are calculated from the Lagrangian droplet variables by

volume averaging the contributions from all of the individual droplets residing within the cell volume ($\delta\mathscr{V} = (\delta x)^3$, where δx is the node spacing) centred around each grid point. In the deforming coordinates, these terms are expressed as

$$\mathscr{S}_m = -\frac{1}{\delta\mathscr{V}} \sum^{n_d} \frac{\mathrm{d}m_d}{\mathrm{d}t}, \tag{22}$$

$$\mathscr{S}_{ui} = -\frac{1}{\delta\mathscr{V}} \sum^{n_d} \left[\frac{m_d f_1}{\tau_d}(u_i^* - v_i) + \frac{\mathrm{d}m_d}{\mathrm{d}t} v_i \right], \tag{23}$$

$$\mathscr{S}_e = -\frac{1}{\delta\mathscr{V}} \sum^{n_d} \left[\frac{\sigma}{(\gamma-1)M_f^2} \frac{\mathrm{d}}{\mathrm{d}t}(m_d T_d) - \frac{\lambda}{(\gamma-1)M_f^2} \frac{\mathrm{d}m_d}{\mathrm{d}t} + \frac{m_d f_1}{\tau_d}(u_i^* - v_i)v_i + \frac{\mathrm{d}m_d}{\mathrm{d}t} \left(\tfrac{1}{2} v_i v_i\right) \right], \tag{24}$$

where $\sigma = 1$ for evaporating droplets. In these equations, n_d is the number of droplets within the cell volume and those cells with $n_d = 0$ are assigned a zero value for each variable.

Equation (22) simply considers the evaporated mass of the droplets as the source term for the carrier-phase continuity and the vapour mass fraction equations. The momentum source terms given in (23) account for the momentum transfer due to drag and the momentum carried to the carrier phase by the evaporated mass. The first term on the right-hand side of (24) is due to the change in the internal energy of the droplets which contributes to the carrier-phase internal energy with a negative sign. By manipulating (7) and (8), it is easy to show that $\mathrm{d}(m_d T_d)/\mathrm{d}t$ represents the exchange of the internal energy by convective heat transfer in addition to the internal energy carried to the carrier phase by vapour. The second term on the right-hand side of (24) subtracts the contribution of the latent heat as the energy equation (3) is described for the sensible internal energy of the carrier phase only. The last two terms on the right-hand side of (24) represent the energy transfer by drag and by the evaporated mass. The exact contributions of these terms to internal and kinetic energies of the carrier phase are discussed in § 4.

It is noted that the source/sink terms described by (22)–(24) reduce to those for non-evaporating droplets (i.e. solid particles) by simply inserting $\mathrm{d}m_d/\mathrm{d}t = 0$. The equations presented in this section for the Eulerian–Lagrangian system are in agreement with the analogous equations presented in the Eulerian–Eulerian framework by Jackson & Davidson (1983).

3. Computational methodology and initializations

Simulations are conducted within the domain $0 \leqslant x_i \leqslant 2\pi$. A Fourier pseudospectral (Givi & Madnia 1993) method with triply periodic boundary conditions is employed for the spatial representation of the carrier-phase variables and the vapour mass fraction. All calculations are performed in Fourier space with the exception of the nonlinear terms. Aliasing errors are treated by truncating energies outside a spherical wavenumber shell having radius $\sqrt{2}N/3$ (where N is the number of grid points in any direction) and time advancement is performed using an explicit second-order-accurate Adams–Bashforth method. The mean shear imposed by the grid transformation skews the grid in time. In order to allow the simulation to progress for a substantial time, it is necessary to remesh the grid at regular time intervals. The remeshing procedure is similar to that used by Rogallo (1981). The grid

begins in an initial orthogonal state and proceeds to skew in the (x_1, x_2)-plane. At a time of $St = 0.5$ the grid is then remeshed back to a hypothetical $St = -0.5$ grid. The fluid variables are then re-calculated onto the new mesh by use of the periodic boundary condition. The choice of time for the remesh process is optimal for the initially cubic domain such that no interpolation is required. After the remeshing, the variables are truncated in Fourier space outside the spherical wavenumber shell of magnitude $\sqrt{2}N/3$. This results in a slight loss of kinetic energy; however, if the simulation is well resolved (i.e. only relatively small energies are present in the highest wavenumber bands) this truncation is considered to be negligible. The simulation is then allowed to proceed until the next remesh time is reached, $St = 0.5, 1.5, 2.5, \ldots$, or until the length scales of the turbulence become too large to be accurately resolved, at which time the simulation is terminated.

As discussed in § 2.3, the dispersed phase is homogeneous within the same domain used for simulating the carrier phase. Once the carrier phase is simulated, the Lagrangian droplet equations are advanced in time using the second-order-accurate Adams–Bashforth method. To evaluate the carrier-phase variables at the droplet location a fourth-order-accurate Lagrange polynomial interpolation scheme is employed. The accuracy of the interpolation scheme has been tested via comparisons made with the exact values calculated using the full spectral description (Balachandar & Maxey 1989). Periodic boundary conditions are applied to the dispersed phase; when a droplet leaves the domain from one side, it is returned to the box from the opposite side. This is possible as the dispersed phase is also homogeneous in the deforming coordinate. Periodicity of the dispersed phase is also used at the time of remeshing to transform the droplets to the new mesh. The X_1- and X_2-coordinates remain the same, whereas $X_1^+ = X_1^- + X_2$ is used to determine the droplet position after remeshing (X_1^+) in terms of its position before remeshing (X_1^-) in the streamwise direction. In evaporating cases, once the droplet time constant falls below 0.1 the droplet is removed from the simulation to avoid excessive computational requirements for tracking very small droplets; no droplet is substituted for the removed droplet. The total number of remaining droplets, however, is monitored to ensure that the Lagrangian statistics are accurate. For all of the cases considered in this study, the total number of droplets used for Lagrangian statistics is always larger than 1.5×10^5. Following Yeung & Pope (1988), the statistical sampling error decreases as $N_d^{1/2}$; using 1.5×10^5 droplets results in less than 0.3% error.

The initial conditions for the flow are fixed for all of the simulations and changes in the flow conditions are only due to interactions with droplets. The density and velocity fields are initialized as random Gaussian, isotropic, and solenoidal fields in Fourier space. The initial temperature field has no fluctuations and the initial pressure field is calculated using the equation of state. The initial spectrum, for both density and velocity, has a box-type shape with non-zero and constant value only for $8 < K < 16$ where K is the wavenumber. The initial mean gas density and mean gas temperature are used as the reference scales for density and temperature, respectively. The reference Mach number is $M_f = 1$; therefore, the speed of sound based on the initial mean gas temperature is the reference scale for the velocity. Other fixed parameters are: $Re_f = 500$, $Pr = Sc = 0.7$, $\gamma = 1.4$, $S = 2$, and $\rho_d = 500$.

The droplets are randomly distributed in the flow at $St = 0$ with the same velocity as that of their surrounding fluid. Different initial temperatures are considered for the droplets in order to study the effects of the temperature difference between the

phases on the flow and the droplets. Both cases of non-evaporating and evaporating droplets are considered with either one- or two-way coupling. For evaporating cases, the droplets begin to evaporate at $St = 2$ when the carrier-phase turbulence kinetic energy starts to grow. The condition of one- or two-way coupling, however, is imposed from $St = 0$ for respective cases. The total number of droplets (N_d) tracked in each simulation is determined from the given values of the droplet time constant and the mass loading ratio. For the one-way coupling case the mass loading ratio is not a relevant parameter. For this case the number of droplets used is the same as that considered for the corresponding two-way coupling case.

The code has been carefully tested by performing the laminar flow test, and by comparisons made with the results of the previous work on single-phase compressible flows by Blaisdell *et al.* (1991). The details of these tests are not presented here for brevity. Also, in the presentation of the results we, frequently, consider the budget of the energy for each of the phases and show that the DNS results accurately balance the left- and right-hand sides of both the kinetic and the internal energy equations. All of the simulations are performed on 96^3 collocation points with a time step of 2.5×10^{-3}, and are continued till the non-dimensional time $St = 14$. The CPU time (on a Cray-C90) is 8.9 s per iteration for evaporating cases in two-way coupling with 3.1×10^5 droplets. The memory required for this case is 46 Mw. We consider the highest possible Reynolds number without jeopardizing the small-scale resolution for all of the fields. The flow field (without the droplets) used for this study has similar characteristics to those simulated by Blaisdell *et al.* (1993) at the same grid resolution and initial r.m.s. turbulence Mach number of 0.2. However, the Reynolds number is smaller in this study – the Taylor-microscale Reynolds number in the streamwise direction varies between ~ 15 at $St = 2$ and ~ 70 at $St = 14$. This is necessary as we are dealing with evaporating droplets and so their sizes decrease to small values in time. As the sizes of the droplets decrease they interact with smaller scales of the flow, therefore it is important to accurately resolve the small scales. This has been ensured by keeping the value of the resolution parameter ηk_{max} (η is the Kolmogorov length scale and k_{max} is the highest wavenumber resolved) larger than 1.4 throughout the simulations.

Due to the large number of parameters involved in the problem, a detailed parametric study is not possible. Instead, we perform a case study to compare the effects of variation of each parameter on the statistics of the flow and the droplets. We consider a 'base case' (indicated by subscript b) for each set of parameters and for each of the other cases within that set we vary one of the parameters with respect to its base value.

4. Non-evaporating droplets

An inspection of the formulation in § 2 identifies the significant parameters for the non-evaporating droplets as the droplet time constant (τ_d), the mass loading ratio (Φ_m), the ratio of the droplet and the carrier-phase specific heats (σ), and the initial droplet temperature (T_{d0}). Table 1 shows a listing of the cases considered to study the effects of these parameters. The base case is indicated with boldface in the table. Also shown in table 1 are values of τ_d/τ_k (τ_k is the Kolmogorov time scale) and d_d/η at $St = 2$ and $St = 13$. For all of the cases, d_d/η varies between 0.2 and 0.3. Therefore, it is reasonable to use Stokes drag equation for the droplets as the flow field around each droplet can be considered uniform. The values of τ_d/τ_k are useful in identifying the scales of the flow which are more effectively interacting with the

τ_d	Φ_m	σ	T_{d0}	Coupling	$N_d \times 10^{-5}$	τ_d/τ_k †	d_d/η †	$\langle\langle Re_d \rangle\rangle$ †
1	**0.1**	**1**	**1**	**2-way**	**1.55**	**2.41 → 1.99**	**0.295 → 0.268**	**0.600 → 0.331**
0.65	0.1	1	1	2-way	2.96	1.57 → 1.32	0.237 → 0.218	0.384 → 0.201
1	0.2	1	1	2-way	3.10	2.40 → 1.89	0.294 → 0.261	0.595 → 0.302
1	0.1	2	1	2-way	1.55	2.41 → 1.99	0.295 → 0.267	0.600 → 0.330
1	0.1	1	0.2	2-way	1.55	2.42 → 1.95	0.295 → 0.265	0.611 → 0.317
1	–	1	1	1-way	1.55	2.43 → 2.14	0.296 → 0.278	0.616 → 0.376

† Values are given at $St = 2$ and $St = 13$.

TABLE 1. Cases considered for the study of non-evaporating droplets. The base case is shown by boldface.

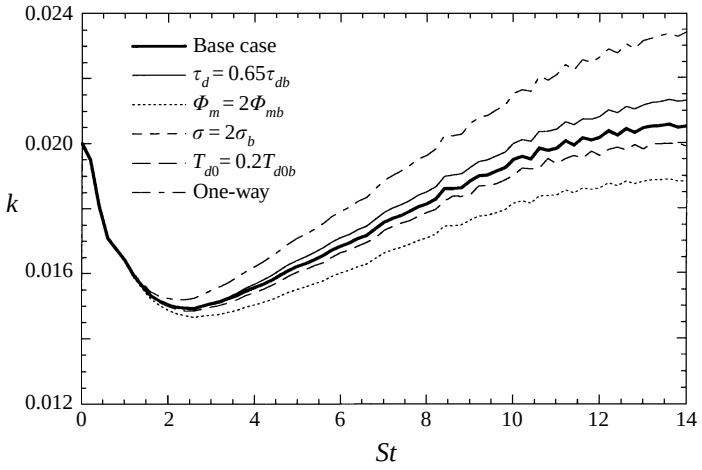

FIGURE 1. Turbulence kinetic energy of the carrier phase for cases with non-evaporating droplets.

droplets (Hinze 1972). Table 1 also shows that the Lagrangian ensemble average ($\langle\langle\ \rangle\rangle$) droplet Reynolds number is less than unity for all of the cases.

4.1. *Velocity fields*

The temporal evolution of the turbulence kinetic energy of the carrier phase ($k = \frac{1}{2}\langle \rho u_i u_i \rangle$) is shown in figure 1. There is an initial decay in the turbulence kinetic energy due to the absence of the off-diagonal (shear) Reynolds stress as the initial velocity field is isotropic. This stress, along with the mean velocity gradient, is responsible for the production of the Reynolds stress in the streamwise direction. Once the shear Reynolds stress component is produced by the action of the mean velocity gradient, the kinetic energy starts to increase ($St > 2$). The primary effect of the droplets is to decrease the carrier-phase turbulence kinetic energy with respect to its single-phase value. In order to explain the trends observed in figure 1, the transport equation for the carrier-phase turbulence kinetic energy (in homogeneous flows) is considered:

$$\frac{\partial k}{\partial t} = \langle p\Delta \rangle + \mathscr{P} - \epsilon + D_d + M_d, \tag{25}$$

where $\langle p\Delta \rangle$ is the pressure–dilatation correlation, $\mathscr{P} = -\langle \rho u_1 u_2 \rangle$ is the production by

the mean velocity gradient, ϵ is the dissipation rate of the turbulence kinetic energy, and

$$D_d = -\left\langle \frac{1}{\delta\mathscr{V}} \sum^{n_d} \left[\frac{f_1 m_d}{\tau_d}(u_i^* - v_i)u_i^* \right] \right\rangle \tag{26}$$

and

$$M_d = -\left\langle \frac{1}{\delta\mathscr{V}} \sum^{n_d} \frac{dm_d}{dt} \left[\tfrac{1}{2}u_i^* u_i^* - (u_i^* - v_i)u_i^* \right] \right\rangle \tag{27}$$

indicate the droplet contributions. Note that for non-evaporating droplets $M_d \equiv 0$. The evolution of the other terms in (25) is discussed below.

First, we consider the pressure–dilatation correlation. This term makes no contribution to the change of the total energy of the carrier phase and it is only responsible for the exchange of energy between kinetic and internal modes. The results of the simulations (not shown) indicated that $\langle p\Delta \rangle$ oscillates in time with relatively large amplitudes; therefore, a clearly observable effect of the pressure–dilatation term is to produce temporal oscillations in the kinetic energy (figure 1). This observation is in agreement with the results of isotropic (stationary or decaying) (Kida & Orsza 1990, 1992), and homogeneous shear (Sarkar 1992) simulations. An inspection of $\langle p\Delta \rangle$ for different cases indicated that, at the same mass loading ratio, the decrease of the droplet time constant slightly decreases the amplitude of the oscillations of $\langle p\Delta \rangle$ at long times. This is despite the fact that in figure 1 the turbulence kinetic energy is larger for the flow laden with smaller droplets, and is due to the presence of a larger number of droplets as compared to the base case. As figure 1 shows, the overall effect of the droplets is to decrease the turbulence fluctuations. The increase of the number of droplets in the flow damps the fluctuations more uniformly in space and results in smaller values for the pressure–dilatation correlation. The increase of the mass loading ratio also tends to diminish the oscillations of the pressure–dilatation correlation due to both the larger number of droplets and the decrease of the velocity fluctuations. The strongest modifications in $\langle p\Delta \rangle$ was observed for the case with small initial droplet temperature for which both the amplitude and the frequency of the oscillations were different than those in the base case. This is expected as the increase of the temperature difference between the droplets and the carrier phase results in local modifications of the density of the carrier phase and increases the spatial variations of the dilatation.

For a constant mean velocity gradient, the production term $\mathscr{P}$ is proportional to the shear Reynolds stress $\langle \rho u_1 u_2 \rangle$. The temporal variation of this stress (normalized with the twice of the turbulence kinetic energy) is shown in figure 2. It is observed that, for cases with the same mass loading ratio, the shear stress decreases proportionally to the decrease of the turbulence kinetic energy. As discussed below, the presence of the droplets increases the total dissipation, which results in a decrease of the velocity fluctuations and, therefore, $\langle \rho u_1 u_2 \rangle$. Figure 2 also indicates that the magnitude of the normalized shear stress decreases with the increase of the mass loading ratio.

Next, we consider the variations of the dissipation rate of the turbulence kinetic energy for different cases. In compressible flows, it is useful to decompose the total dissipation rate (ϵ) into incompressible (ϵ_I) and compressible (ϵ_C) parts which are defined as

$$\epsilon_I = \frac{1}{Re_f}\langle \omega_i \omega_i \rangle, \quad \epsilon_C = \frac{4}{3}\frac{1}{Re_f}\langle \Delta^2 \rangle, \tag{28}$$

where ω_i is the fluctuating vorticity vector. Figure 3 shows the temporal variations

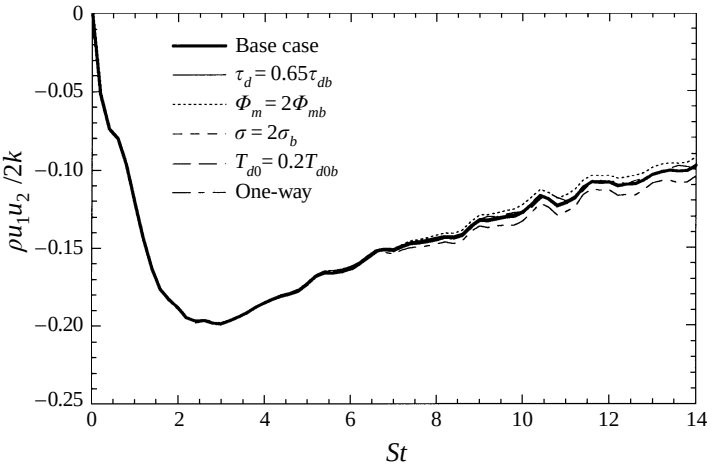

FIGURE 2. Normalized shear stress of the carrier phase.

of the total dissipation and its compressible part. These quantities are normalized by the total dissipation (ϵ_1) of the clean (droplet-free) flow. In this manner, the deviation of ϵ/ϵ_1 from unity is a measure of the total effect of the droplets on the dissipation rate. Notice that the curves for ϵ_C/ϵ_1 have been shifted by 0.3 to avoid confusion with the curves for D_d/ϵ_1. Both the total dissipation rate and its compressible part decrease with the increase of the mass loading ratio. This is due to the decrease of the velocity fluctuations with the increase of the mass loading ratio. An interesting phenomenon observed in figure 3 is the increase of the compressible (and, therefore, the total) dissipation rate during the early times for the case with the smaller initial droplet temperature. This is due to the increase of the spatial fluctuations of the velocity dilatation in this case. The initial increase of the dissipation rate explains the smaller growth rate of the turbulence kinetic energy for the case with small initial droplet temperature (figure 1).

Also shown in figure 3 are the temporal variations of the term D_d which indicates the effects of drag. It is observed that the increase of the mass loading ratio results in a significant increase in the magnitude of D_d during the early stages. Therefore, the total dissipation (due to both the carrier-phase velocity field (ϵ) and the droplet interaction (D_d)) increases. This explains the decrease of the growth rate of the turbulence kinetic energy with the increase of the mass loading ratio. The decrease of the droplet time constant, at the same mass loading ratio, results in the decrease of the magnitude of D_d. It is also observed in figure 3 that, at long times, D_d takes positive values indicating that the droplets tend to enhance the turbulence kinetic energy of the carrier phase. To explain this phenomenon, D_d is described in terms of Lagrangian correlations. Assuming a negligible correlation between the fluctuations of f_1 and second-order velocity fluctuations ($u_i^* u_i^*$ and $u_i^* v_i$) and noting that $\Phi_m = N_d m_d/(N\delta\mathscr{V})$, it is easy to show that

$$D_d \simeq -\Phi_m \frac{\langle\langle f_1 \rangle\rangle}{\tau_d}(\langle\langle u_i^* u_i^* \rangle\rangle - \langle\langle u_i^* v_i \rangle\rangle). \tag{29}$$

A comparison of D_d values calculated by (26) and (29) indicated that, for the simulations considered here, these two relations are virtually the same.

The temporal variations of the components of $\langle\langle u_i^* u_i^* \rangle\rangle$ and $\langle\langle v_i v_i \rangle\rangle$ are portrayed in figure 4 for different values of the droplet time constant and the mass loading

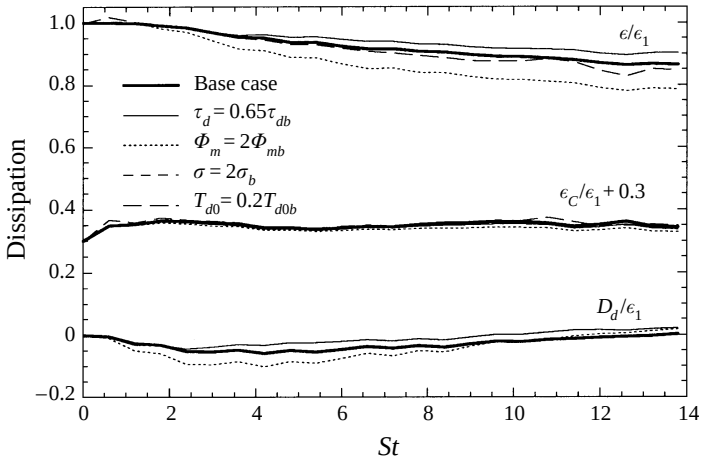

FIGURE 3. Temporal variations of the dissipation rate (ϵ) of the carrier phase and its compressible part (ϵ_C). Also shown on the figure is the variation of the drag contribution (D_d) to the carrier-phase turbulence kinetic energy. All of these parameters are normalized with the dissipation rate (ϵ_1) from the case with one-way coupling.

ratio. The variation of the spanwise (x_3-direction) component is similar to that of the cross-stream (x_2-direction) component and is not shown on the figure. Figure 4 shows that the streamwise component of the droplet Reynolds stress is significantly larger than that of the carrier phase. This may suggest that the term $\langle\langle u_i^* v_i \rangle\rangle$ should be larger than the term $\langle\langle u_i^* u_i^* \rangle\rangle$ in (29) and D_d should be positive throughout the simulations. However, in calculating $\langle\langle u_i^* v_i \rangle\rangle$, the alignment of the droplet velocity with the carrier phase velocity must be considered. A measure of this alignment is: $\cos(u_i^*, v_i) = \langle\langle u_i^* v_i \rangle\rangle / (\langle\langle (u_i^*)^2 \rangle\rangle \langle\langle v_i^2 \rangle\rangle)^{1/2}$ which is shown in figure 5 for different cases. This figure indicates that during the early times, u_i^* and v_i become largely uncorrelated resulting in the decrease of $\langle\langle u_i^* v_i \rangle\rangle$ to values smaller than $\langle\langle u_i^* u_i^* \rangle\rangle$. This behaviour is due to rapid evolution of the flow field during the early times. The droplets (having large inertia), however, are not capable of promptly responding to these changes in the flow. For the same reason, the droplets with smaller time constant exhibit a better alignment with the carrier phase. At long times, the flow field is in an equilibrium state and it is easier for the droplets to follow the fluid motions, therefore the magnitude of $\cos(u_i^*, v_i)$ increases.

As mentioned earlier, an interesting feature observed in figure 4 is the increase of the droplet Reynolds stress in the x_1-direction over that of the carrier phase. This is in agreement with theoretical results of Reeks (1993) and Liljegren (1993) and the LES results of Simonin *et al.* (1995) (in incompressible turbulence), and is due to lack of small-scale dissipation in the dispersed phase as opposed to the carrier phase. In the x_2-direction a crossing point is observed for the curves shown on figure 4 at $St \simeq 3$. The reason is that, at early times, the dispersed-phase Reynolds stress decreases slower than the fluid one, due to the droplet inertia and small-scale dissipation in the fluid. At longer times ($St > 3$), the fluid pressure transfers energy from the streamwise direction to other directions and causes the increase of the fluid Reynolds stress in the x_2-direction over that of the droplets. It is also shown in the figure that the large initial values of $\langle\langle v_2 v_2 \rangle\rangle$ result in large production of the shear component for the dispersed phase and increases the magnitude of this component to values larger than those of the fluid. The effect of two-way coupling is realized by comparison of

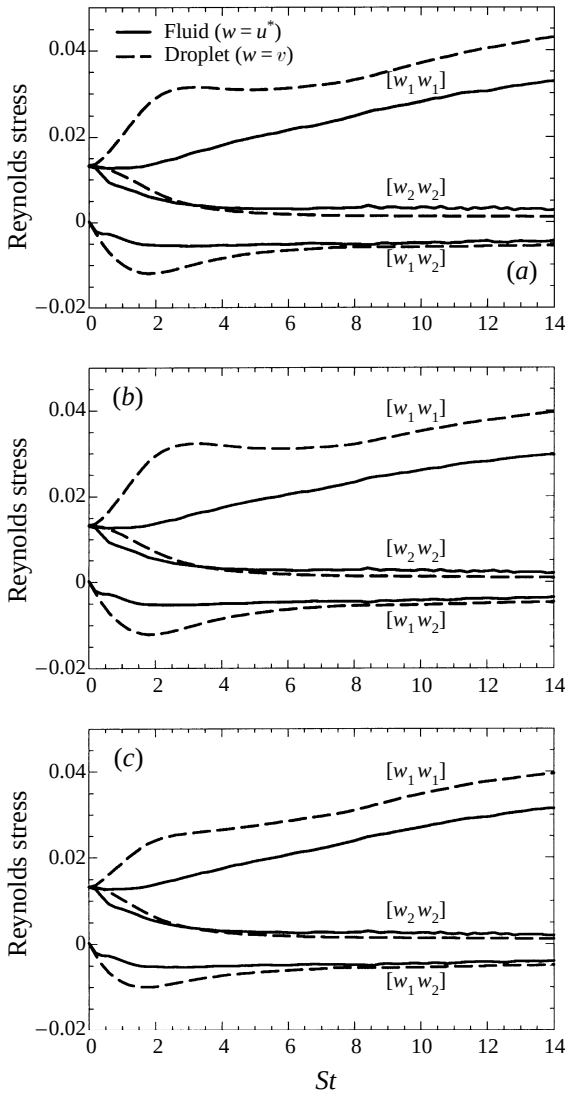

FIGURE 4. Reynolds stress components for the carrier phase and the droplets from non-evaporating cases: (*a*) $\tau_d = 1$, one-way coupling, (*b*) $\tau_d = 1$, $\Phi_m = 0.1$, and (*c*) $\tau_d = 0.65$, $\Phi_m = 0.1$. For the carrier phase $[w_i w_j] \equiv \langle\langle u_i^* u_j^* \rangle\rangle$ and for the droplets $[w_i w_j] \equiv \langle\langle v_i v_j \rangle\rangle$.

figures 4(*a*) and 4(*b*). The trends are the same in the two figures; however, at long times the difference between the normal components of the Reynolds stress of the dispersed phase is smaller in two-way coupling, due to the indirect effects of the fluid pressure. Figure 4 (*c*) indicates that the variation of the droplet time constant also has strong effects on the Reynolds stress components. Again, in agreement with previous observations in incompressible flow (Mashayek, Taulbee & Givi 1998*a*), the decrease of the droplet time constant results in the decrease of the ratio of the droplet Reynolds stress to that of the fluid in the streamwise direction. This is in contrast to the increase of this ratio with the decrease of the droplet time constant in isotropic flows.

In order to gain further insight into the evolution of the droplet Reynolds stress,

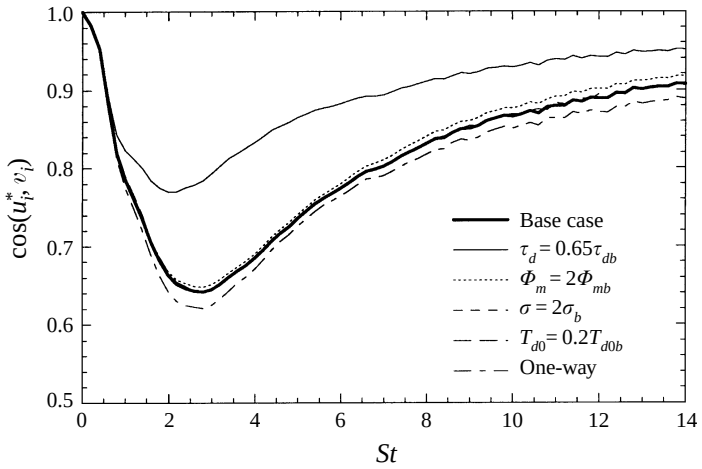

FIGURE 5. Alignment of the velocity of the droplets with the velocity of the carrier phase.

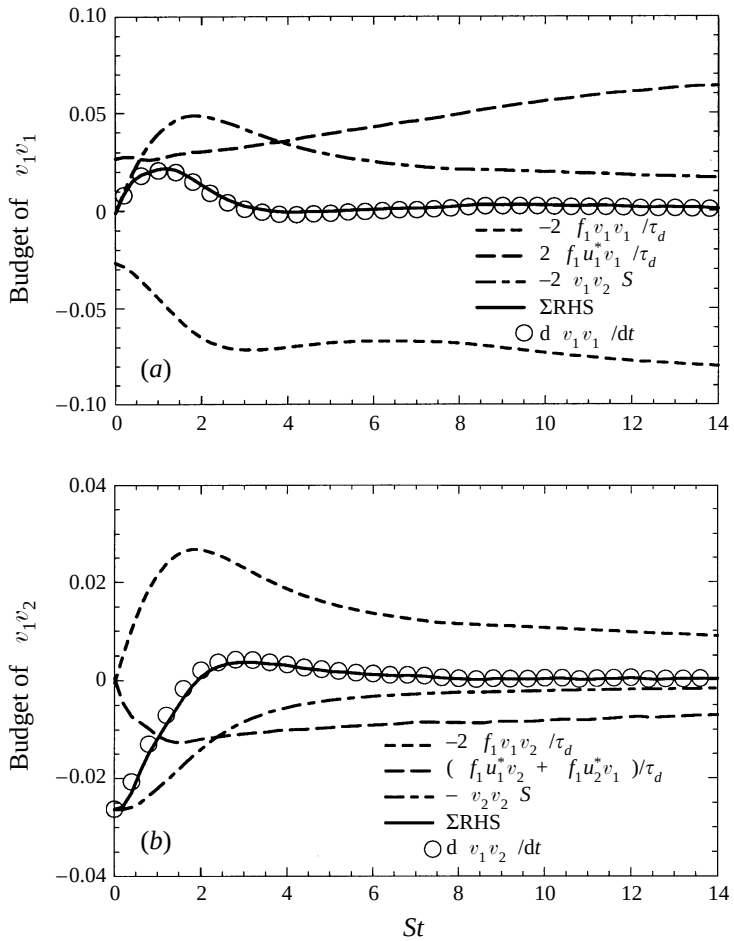

FIGURE 6. Budgets of (*a*) the streamwise and (*b*) the shear Reynolds stresses of the droplets in the non-evaporating case with $\tau_d = 1$ and $\Phi_m = 0.2$.

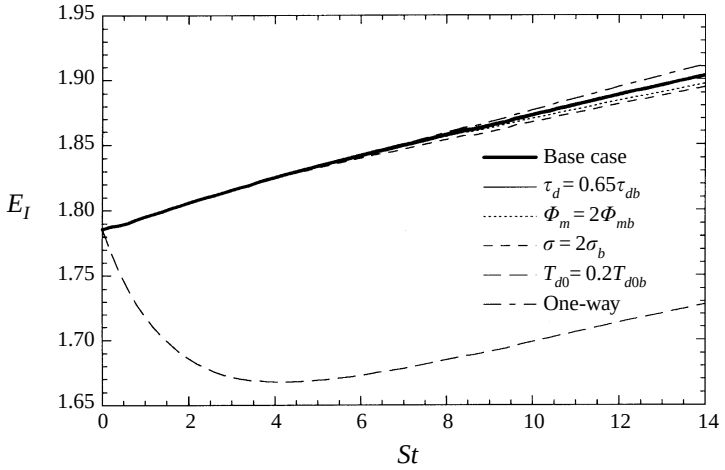

FIGURE 7. Mean internal energy of the carrier phase for non-evaporating cases.

we consider the transport equation for $\langle\langle v_i v_j \rangle\rangle$. This transport equation is obtained from (21), and in deforming coordinates it reads

$$\frac{\mathrm{d}}{\mathrm{d}t}\langle\langle v_i v_j \rangle\rangle = -\langle\langle v_i v_2 \rangle\rangle S\delta_{1j} - \langle\langle v_2 v_j \rangle\rangle S\delta_{i1} + \left[\left(\left\langle\left\langle \frac{f_1}{\tau_d} u_i^* v_j \right\rangle\right\rangle + \left\langle\left\langle \frac{f_1}{\tau_d} u_j^* v_i \right\rangle\right\rangle\right) - 2\left\langle\left\langle \frac{f_1}{\tau_d} v_i v_j \right\rangle\right\rangle\right]. \quad (30)$$

Figure 6 shows the budget of the streamwise and shear components of the droplet Reynolds stress for the case with $\tau_d = 1$ and $\Phi_m = 0.2$. The transport equations for these components are

$$\frac{\mathrm{d}}{\mathrm{d}t}\langle\langle v_1 v_1 \rangle\rangle = -2\langle\langle v_1 v_2 \rangle\rangle S + 2\left(\left\langle\left\langle \frac{f_1}{\tau_d} u_1^* v_1 \right\rangle\right\rangle - \left\langle\left\langle \frac{f_1}{\tau_d} v_1 v_1 \right\rangle\right\rangle\right), \quad (31)$$

$$\frac{\mathrm{d}}{\mathrm{d}t}\langle\langle v_1 v_2 \rangle\rangle = -\langle\langle v_2 v_2 \rangle\rangle S + \left[\left(\left\langle\left\langle \frac{f_1}{\tau_d} u_1^* v_2 \right\rangle\right\rangle + \left\langle\left\langle \frac{f_1}{\tau_d} u_2^* v_1 \right\rangle\right\rangle\right) - 2\left\langle\left\langle \frac{f_1}{\tau_d} v_1 v_2 \right\rangle\right\rangle\right]. \quad (32)$$

Based on the results shown in figure 6, production by the mean velocity gradient plays a significant role (especially during the early times) in the evolution of the droplet Reynolds stresses. At long times, the production is mostly compensated by the contribution from the drag, and the Reynolds stresses grow with small rates. Figure 6 (*a*) also indicates that the initial growth of $\langle\langle v_1 v_1 \rangle\rangle$ is largely decreased by the decorrelation of the fluid and the droplet velocities during the early times (figure 5). Therefore, sudden changes in the mean velocity gradient significantly affects both the production and the drag contribution on the right-hand side of (30).

4.2. *Thermodynamic fields*

The evolution of various thermodynamic fields is considered in this subsection. Figure 7 shows the temporal variation of the mean internal energy of the carrier phase. It is observed that the mean internal energy is not sensitive to the droplet size but is affected by changes in the other parameters. As expected, the largest variations in $\langle E_I \rangle$ occur for the case with small initial droplet temperature. In this case, the mean internal energy of the carrier phase initially decreases due to heat transfer with

the droplets which are at much smaller temperature than that of the carrier phase. After the droplets are heated to temperatures close to the carrier-phase temperature, the mean internal energy of the carrier phase begins to increase with a rate close to those in other cases.

To assess the relative importance of various mechanisms involved in the change of the internal energy of the carrier phase we consider the transport equation for $\langle E_I \rangle$ in homogeneous flows:

$$\frac{\partial \langle E_I \rangle}{\partial t} = -\langle p \Delta \rangle + \epsilon + \frac{S^2}{Re_f} + Q_d + H_d + \Phi_d + \Theta_d, \tag{33}$$

where $S^2/Re_f = 0.008$ is the dissipation due to the mean velocity gradient. For the cases considered here this term has about the same magnitude as ϵ. It is noted that this term only appears in the transport equation for the mean internal energy, and not in the transport equation for the turbulence kinetic energy of the carrier phase. It represents the effects of the mean velocity gradient on heat and mass transfer. Since S^2/Re_f is a positive quantity, it always increases the internal energy (and the temperature) of the carrier phase, thus enhancing the rate of heat and mass transfer between the phases.

The dispersed-phase contributions to the mean internal energy of the carrier phase are expressed as

$$Q_d = -\left\langle \frac{\sigma}{(\gamma-1)M_f^2 \delta \mathscr{V}} \sum^{n_d} m_d \frac{\mathrm{d}T_d}{\mathrm{d}t} \right\rangle, \tag{34}$$

$$H_d = -\left\langle \frac{\sigma}{(\gamma-1)M_f^2 \delta \mathscr{V}} \sum^{n_d} \frac{\mathrm{d}m_d}{\mathrm{d}t} T_d \right\rangle, \tag{35}$$

$$\Phi_d = \left\langle \frac{1}{\delta \mathscr{V}} \sum^{n_d} \frac{f_1 m_d}{\tau_d} (u_i^* - v_i)^2 \right\rangle, \tag{36}$$

and

$$\Theta_d = -\left\langle \frac{1}{\delta \mathscr{V}} \sum^{n_d} \frac{1}{2} \frac{\mathrm{d}m_d}{\mathrm{d}t} (u_i^* - v_i)^2 \right\rangle, \tag{37}$$

where $\sigma = 1$ and $E_I = \rho(T/\gamma + Y\lambda)/(\gamma-1)M_f^2$ for evaporating droplets. For non-evaporating droplets $m_d = \text{const.}$, therefore $H_d \equiv 0$ and $\Theta_d \equiv 0$. In this case, Q_d represents the convective heat transfer between the two phases, and is exactly expressed in terms of the Lagrangian ensemble average of the droplet temperature:

$$Q_d = -\frac{\sigma}{(\gamma-1)M_f^2} \Phi_m \frac{\mathrm{d}\langle\langle T_d \rangle\rangle}{\mathrm{d}t}. \tag{38}$$

The term Φ_d represents the viscous dissipation due to drag. It is noted that Φ_d contributes to the change of the internal energy and is distinguished from the contribution of the drag force to the kinetic energy, D_d. The former is due to the drag force deforming the fluid elements surrounding the droplet while the latter is the result of the drag force directly accelerating the fluid. A physical explanation for Φ_d follows. In general, the contribution of the fluid stress to the internal energy is given by $\tau_{ij}\partial u_j/\partial x_i$ (Panton 1984), where τ_{ij} is the stress tensor. For a droplet moving relative to a fluid, the average stress is given by the drag force per unit area

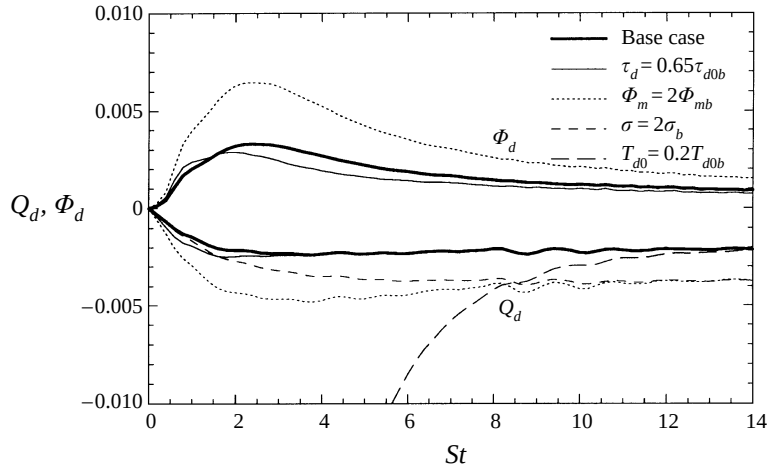

FIGURE 8. Rate of change of the mean carrier-phase internal energy by convective heat transfer with the droplets (Q_d) and by drag dissipation (Φ_d).

of the droplet surface, and $\partial u_j/\partial x_i$ can be approximated by the velocity difference $(u_i^* - v_i)$ divided by the thickness of the boundary layer formed around the droplet. The product of the droplet surface area and the thickness of the boundary layer is, in fact, the volume within which the dissipation takes place. In accord with the numerical approximation in which the effects of a droplet on the fluid are modelled as a source term for the cell containing the droplet, this volume may be substituted by the cell volume. Therefore, the viscous dissipation due to one droplet is approximated by the product of the drag force and the local velocity difference $(u_i^* - v_i)$ divided by the cell volume. Now, summing over the number of droplets within the cell, Φ_d takes the expression given by (36). A Lagrangian relation for Φ_d is possible by assuming that there is only a weak correlation between the fluctuations of f_1 and $(u_i^* - v_i)^2$:

$$\Phi_d \simeq \Phi_m \frac{\langle\langle f_1 \rangle\rangle}{\tau_d} \langle\langle (u_i^* - v_i)^2 \rangle\rangle. \tag{39}$$

The temporal variations of Q_d and Φ_d are portrayed in figure 8. With the exclusion of Q_d for the case with small initial droplet temperature, the magnitude of both Q_d and Φ_d varies between zero and 0.007. During the early times, these terms are of the same order of significance as the dissipation terms in (33); however, contrary to the dissipation terms, Q_d and Φ_d have opposite signs and tend to cancel each other. The fact that Φ_d is of the same order of magnitude as the dissipation rate should not be overlooked and suggests that this term must be included in the modelling of two-phase flows. Based on the results shown in figure 8, Φ_d is only sensitive to the variations of the droplet time constant and the mass loading ratio. This is expected as none of the thermodynamic variables (directly) appear in the relation for Φ_d. The increase of the mass loading ratio from 0.1 to 0.2 has almost doubled the magnitude of Φ_d, suggesting a nearly linear variation with the mass loading ratio for Φ_d in the range of small to moderate Φ_m. Except for a short initial period, the decrease of the droplet time constant lessens Φ_d due to the decrease of the relative velocity between the phases. As expected, Q_d is very sensitive to thermodynamic variables. The increase of the droplet specific heat increases the heat transfer from the carrier phase to the droplets and results in the increase of Q_d. A similar effect is observed for the mass

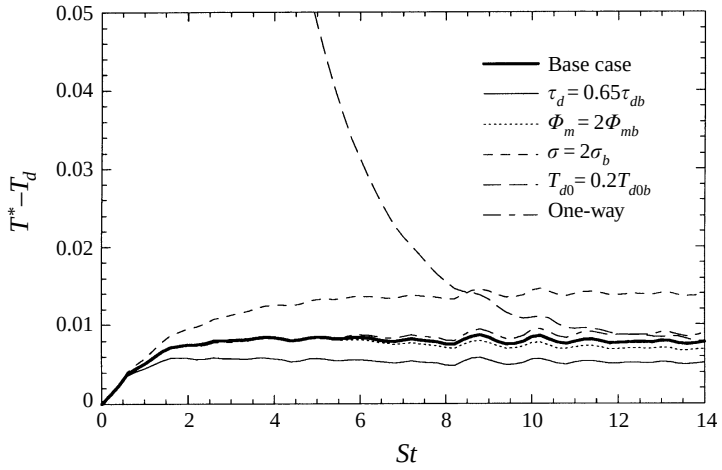

FIGURE 9. Mean temperature difference between the carrier phase and the droplets.

loading ratio as the increase of this parameter also increases the total heat transfer from the carrier phase to the droplets. It is noted that, at long times, Q_d becomes independent of the initial droplet temperature.

More insight into heat transfer between the carrier phase and the droplets is possible by analysing the variations of the mean temperature difference. Figure 9 shows that $\langle\langle T^* - T_d \rangle\rangle$ is always positive, indicating a net heat transfer from the carrier phase to the droplets. As was shown earlier, the mean internal energy of the carrier phase increases in time due to dissipation terms and Φ_d, therefore the temperature of the carrier phase is larger than that of the dispersed phase. This creates a net heat transfer from the carrier to the dispersed phase. It appears that for all of the cases the mean temperature difference approaches some asymptotic value at long time. Interestingly, this asymptotic value is independent of the initial temperature difference between the phases. It shows a small sensitivity to the mass loading ratio and decreases with the increase of this parameter, due to modifications of the carrier phase by the droplets in two-way coupling. The decrease of the droplet time constant decreases the temperature difference as smaller droplets have smaller heat capacity. For a similar reason, the increase of the droplet specific heat results in the increase of the mean temperature difference. These trends are similar to those observed for variations of the mean relative velocity with the droplet time constant in isotropic flows. This is expected since for a thermal system the heat capacity (the product of the mass and the specific heat) plays the same role as inertia plays for aerodynamics.

From a modelling standpoint, the r.m.s. of the temperature fluctuation of both the carrier and the dispersed phases are of great interest as knowledge of these quantities suffices to determine the mean values for the temperature. The temporal variations of $T_{rms} = (\langle (T - \langle T \rangle)^2 \rangle)^{1/2}$ and $T_{drms} = (\langle\langle (T_d - \langle\langle T_d \rangle\rangle)^2 \rangle\rangle)^{1/2}$ are shown in figure 10. Similarly to the mean temperature difference, the r.m.s. of the temperature fluctuation approaches asymptotic values at long times. For all of the cases, the r.m.s. fluctuating temperature of the carrier phase is larger than that of the droplets. This is due to larger heat capacity of the droplets and is analogous to variations of the r.m.s. of the droplet velocity with the droplet inertia in isotropic flows. The asymptotic values of the r.m.s. of the carrier-phase temperature fluctuation are more sensitive to variations of the mass loading ratio than to variations of the other parameters.

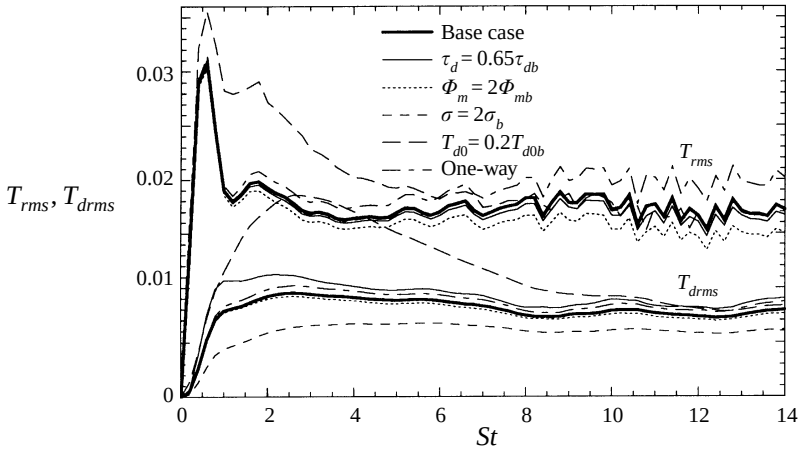

FIGURE 10. The r.m.s. of fluctuating temperatures of the carrier phase and the droplets for non-evaporating cases.

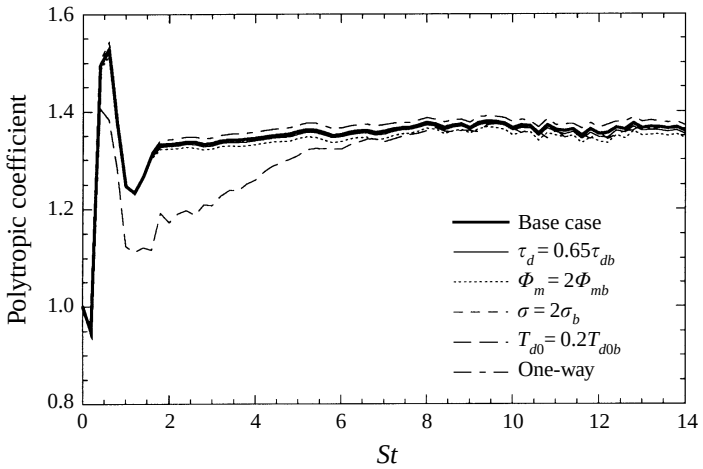

FIGURE 11. The polytropic coefficient for non-evaporating cases.

The long-time values of the r.m.s. of the droplet temperature fluctuation, however, appears to be more dependent on the droplet time constant and the droplet specific heat coefficient. A comparison of the r.m.s. temperature fluctuations for the base case and the case with small initial droplet temperature indicates that the r.m.s. values become independent of the initial conditions at long time.

Also of great interest in the modelling of compressible flows is the relation among the fluctuations of the thermodynamic variables. A common approach is to relate the fluctuating values of the density, the temperature, and the pressure through a polytropic coefficient (Rubesin 1976). The local values of the polytropic coefficient, however, are not well-defined as it is possible that the fluctuating density or the fluctuating pressure independently take zero values. To remove the singularity, Blaisdell *et al.* (1993) propose an average value for the polytropic coefficient:

$$n = \frac{(\langle (P - \langle P \rangle)^2 \rangle)^{1/2} / \langle P \rangle}{(\langle (\rho - \langle \rho \rangle)^2 \rangle)^{1/2} / \langle \rho \rangle}. \tag{40}$$

τ_{d0}	Φ_{m0}	λ	T_B	Y_0	T_{d0}	Evaporation
1	**0.1**	**0.8**	**2**	**0**	**1**	**Yes**
0.65	0.1	0.8	2	0	1	Yes
1	0.2	0.8	2	0	1	Yes
1	0.1	2	2	0	1	Yes
1	0.1	0.8	5	0	1	Yes
1	0.1	0.8	2	0.1	1	Yes
1	0.1	–	–	–	1	No

TABLE 2. Cases considered for the study of evaporating droplets. All of the cases are with two-way coupling. The base case is shown by boldface.

The temporal variations of n are shown in figure 11. It is observed that after an initial transient period the polytropic coefficient becomes stationary in time. It shows small sensitivity to the changes in each of the parameters, although it is more sensitive to the mass loading ratio. For all of the cases, the asymptotic value of the polytropic coefficient is between 1.35 and 1.38 which is close to $n = \gamma = 1.4$ for an isentropic flow. The addition of the droplets to the flow always decreases the polytropic coefficient as the heat transfer between the droplets and the gas takes place at finite temperature differences. This increases the irreversibilities and causes deviations from an isentropic flow.

5. Evaporating droplets

A listing of cases considered for the investigation of dispersion and polydispersity of the evaporating droplets is provided in table 2. The significant parameters for evaporating droplets are the initial droplet time constant (τ_{d0}), the initial mass loading ratio (Φ_{m0}), the normalized droplet latent heat of evaporation (λ), the boiling temperature (T_B), the initial vapour mass fraction (Y_0, considered to be uniform in space), and the initial droplet temperature (T_{d0}). The case with $Y_0 = 0.1$ is initialized in such a way that the initial mean carrier-phase density remains the same as in other cases (i.e. $\langle\rho\rangle = 1$ at $St = 0$); the mean density of the gas alone is 0.9 for this case. For all of the cases in table 2 the initial droplet temperature is the same as that of the carrier phase (i.e. $T_{d0} = 1$). The effects of the initial temperature of the droplets will be studied separately in § 5.4. All of the cases are with two-way coupling. The base case here is the same as the one considered in § 4 but for evaporating droplets. The droplets are injected into the flow at $St = 0$; however, evaporation starts at $St = 2$, after the droplets reach some dynamic equilibrium with the carrier phase. It is emphasized again that the carrier phase consists of both the gas and the vapour.

5.1. *Velocity fields*

We begin our discussion on evaporating droplets by considering the temporal variations of the carrier-phase turbulence kinetic energy shown in figure 12. When analysing the trends observed in figure 12, it is important to distinguish between $k = \frac{1}{2}\langle\rho u_i u_i\rangle$ and the parameter $\frac{1}{2}\langle u_i u_i\rangle$ as the former includes the density effects as well. The evolution of the turbulence kinetic energy is affected by evaporation in two ways. (i) Evaporation decreases the mass loading ratio which in turn results in the decrease of the effects of the drag on the carrier phase. As was observed in § 4.1, during the early stages of the flow evolution, the drag term tends to act as a dissipation term. Thus,

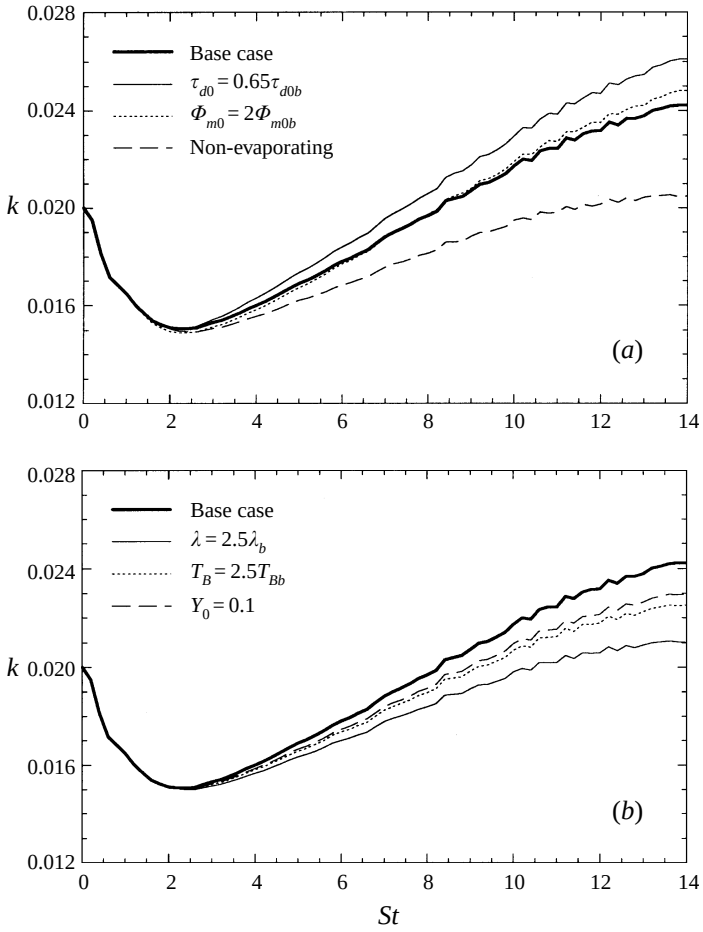

FIGURE 12. The carrier-phase turbulence kinetic energy for evaporating cases.

evaporation decreases the total dissipation and tends to enhance the growth rate of the turbulence kinetic energy of the carrier phase. This is also true for the velocity variance $\langle u_i u_i \rangle$. (ii) Evaporation results in mass (and kinetic energy) transfer from the droplets to the carrier phase. This always increases the mass-weighted kinetic energy as defined in figure 12. However, the velocity variance of the carrier phase may either increase or decrease depending on the relative magnitudes of the velocities of the two phases. Since both of the above mechanisms result in the increase of k, it is not surprising that in figure 12 all of the evaporating cases exhibit larger turbulence kinetic energies than that of the non-evaporating case.

Further insight into the evolution of the carrier-phase turbulence kinetic energy is gained by analysing the temporal variations of the droplet source/sink terms in the transport equation (25) for k. These terms, labelled D_d and M_d, represent mechanisms (i) and (ii) above, respectively. The temporal variations of D_d and M_d are shown in figure 13 for different cases. To assess the significance of these terms, it is instructive to compare their magnitudes with the magnitude of $\partial k/\partial t$ on the left-hand side of (25). From figure 12 it is estimated that, for $2 < St < 14$, $\partial k/\partial t \simeq 0.0015$ which is of the same order of magnitude as D_d and M_d during the initial times. The results in figure 13 indicate that D_d and M_d are of opposite signs, therefore the kinetic energy

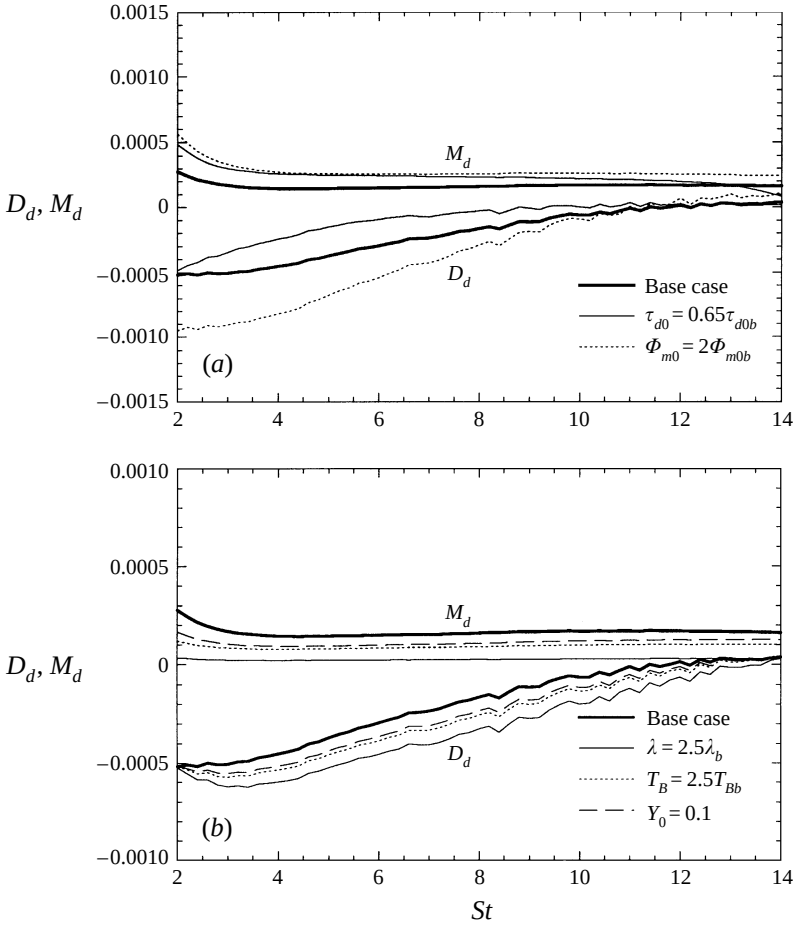

FIGURE 13. Rate of change of the carrier-phase turbulence kinetic energy by drag (D_d) and by mass transfer (M_d).

transferred to the carrier phase by the evaporated mass tends to compensate the effects of the drag of the droplets and the evaporating cases behave more analogously to the one-way coupling case rather than the non-evaporating two-way coupling case at the same initial droplet time constant. The relative importance of D_d and M_d directly depends on the rate of evaporation: for cases with small evaporation rate (e.g. the case with $\lambda = 2.5\lambda_b$), M_d is less significant than D_d. In general, as the evaporation rate increases the kinetic energy of the carrier phase also increases. A discussion on the rate of evaporation is provided later in § 5.3.

The presence of the droplets in the carrier phase is expected to affect the anisotropy of the flow as the droplets are shown to be more anisotropic than the carrier phase. Figure 14 shows the temporal evolution of the normalized normal Reynolds stresses of the carrier phase (no sum on Greek indices) for three different cases. A comparison of the case with two-way coupling for non-evaporating droplets with the one-way coupling case ($\Phi_m = 0$) clearly shows that the anisotropy of the carrier phase is increased by the presence of the droplets. However, it appears that at long times the rates of change of the normalized stresses are the same for cases with or without droplets. Evaporation tends to decrease the level of anisotropy (caused by the droplets)

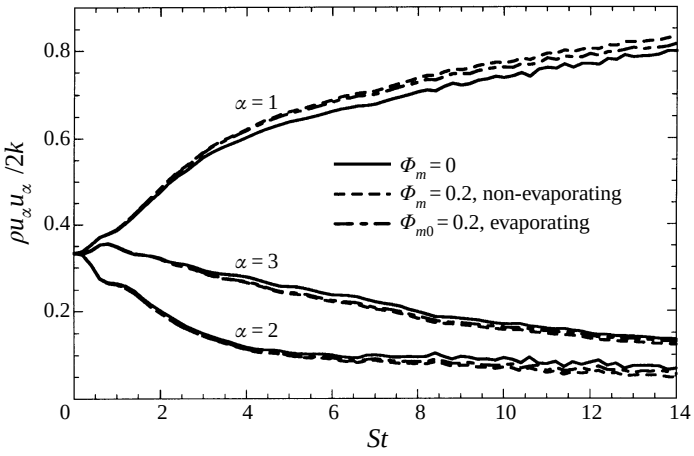

FIGURE 14. Anisotropy of the carrier-phase Reynolds stresses.

at long times. This is mainly due to the decrease of the effects of the droplets on the carrier phase as the mass loading ratio decreases in time.

From the modelling point of view it is always desirable to describe the higher-order correlations in terms of the lower-order correlations. For instance, the transport equation for the turbulence kinetic energy of the droplets involves correlations between the modified droplet time constant and the velocity fluctuations such as $\langle\langle (f_1/\tau_d) u_i^* v_i \rangle\rangle$. This correlation may be described in terms of the first- and the second-order moments, i.e. $(\langle\langle f_1 \rangle\rangle / \langle\langle \tau_d \rangle\rangle)\langle\langle u_i^* v_i \rangle\rangle$, where $\langle\langle f_1 \rangle\rangle$ is calculated using $\langle\langle Re_d \rangle\rangle$ and $\langle\langle B \rangle\rangle$. In this manner, the drag contribution in the droplet kinetic energy equation may be approximated as

$$\left\langle\left\langle \frac{f_1}{\tau_d}\left[(u_i^* v_j + u_j^* v_i) - 2 v_i v_j\right]\right\rangle\right\rangle \simeq \frac{\langle\langle f_1 \rangle\rangle}{\langle\langle \tau_d \rangle\rangle}\left[(\langle\langle u_i^* v_j \rangle\rangle + \langle\langle u_j^* v_i \rangle\rangle) - 2\langle\langle v_i v_j \rangle\rangle\right]. \tag{41}$$

In order to examine (41), in figure 15 we consider the budget of the streamwise (31) and shear (32) Reynolds stresses of the dispersed phase for a typical case with $\tau_{d0} = 1$ and $\Phi_{m0} = 0.2$. A very close agreement between the left-hand side (circles) and the sum of the terms on the right-hand side (solid line) is observed in the figure. This indicates that the assumption made in (41) is reasonable for practical purposes. It is also useful to compare the curves in figure 15 to analogous curves presented earlier in figure 6 for non-evaporating droplets at the same droplet time constant and mass loading ratio. It appears that the production term does not change significantly; however, the magnitude of the terms pertaining to drag is greatly increased in time as a result of the decrease of the droplet size.

5.2. *Thermodynamic fields*

The temporal evolution of the mean internal energy of the carrier phase ($\langle E_I \rangle$) is shown in figure 16. For cases with evaporating droplets, $\langle E_I \rangle$ includes the internal energies of both the gas and the vapour, and, unlike in non-evaporating cases, it is not linearly proportional to the temperature of the carrier phase. Figure 16 shows that the mean internal energy of the carrier phase for evaporating cases is always larger than that for non-evaporating cases. The increase of the mass loading ratio or the decrease of the droplet time constant increases the mean internal energy by increasing the mass of the vapour. A similar argument also applies to figure 16(*b*) which shows the effects of the variations of λ, T_B, and Y_0; the case with higher

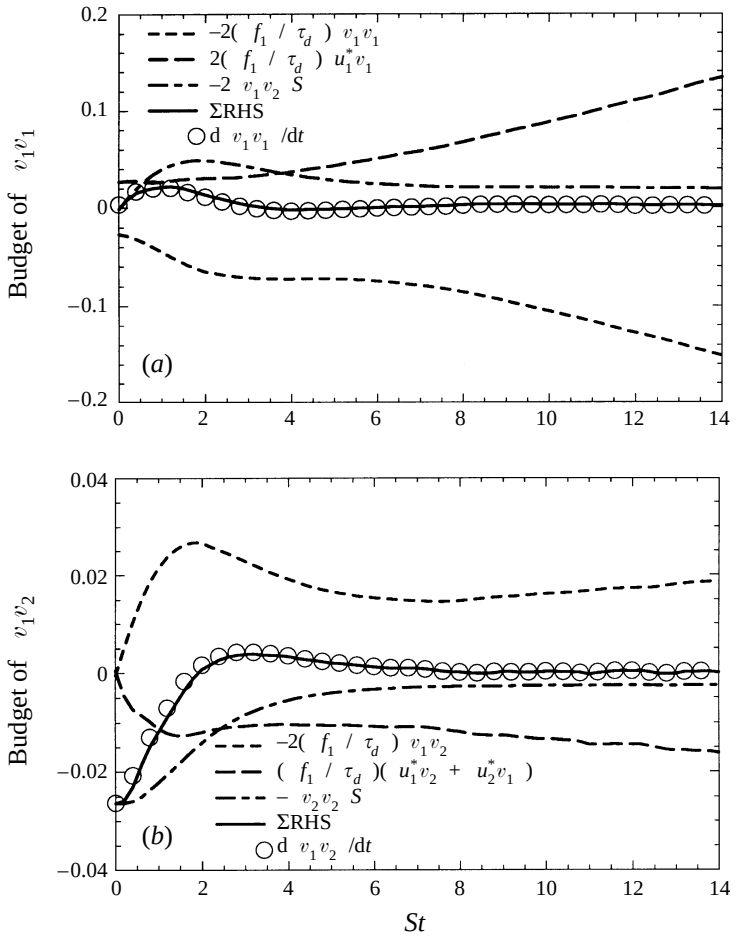

FIGURE 15. Budgets of (*a*) the streamwise and (*b*) the shear Reynolds stresses of the droplets in the evaporating case with $\tau_{d0} = 1$ and $\Phi_{m0} = 0.2$.

evaporation rate exhibits a higher mean internal energy. Notice that the initial mean internal energy for the case with $Y_0 = 0.1$ is larger than that for other cases as in this case a portion of the initial mass of the carrier phase is composed of vapour which has larger specific enthalpy.

In order to identify the mechanisms by which the droplets most effectively influence the internal energy of the carrier phase, the budget of the mean internal energy (equation (33)) is considered. Figure 17 shows the temporal variations of various terms in (33) for a typical case with $\tau_{d0} = 1$ and $\Phi_{m0} = 0.2$; other cases show similar trends. After the onset of evaporation ($St > 2$), the fate of the mean internal energy is mostly determined by the internal energy transferred by the vapour to the carrier phase, H_d. For a short period after evaporation begins ($2 < St < 4$) the term Q_d also plays a significant role. At long times, Q_d is very small and the internal energy generated by small-scale dissipation in the fluid becomes of the same order of importance as H_d. According to the results shown in figure 17, for evaporating cases, the dissipation due to the droplet drag (Φ_d) and the internal energy due to velocity difference between the two phases (Θ_d) are small compared to other terms. Due to the importance of Q_d and H_d in analysing the mean internal energy of the

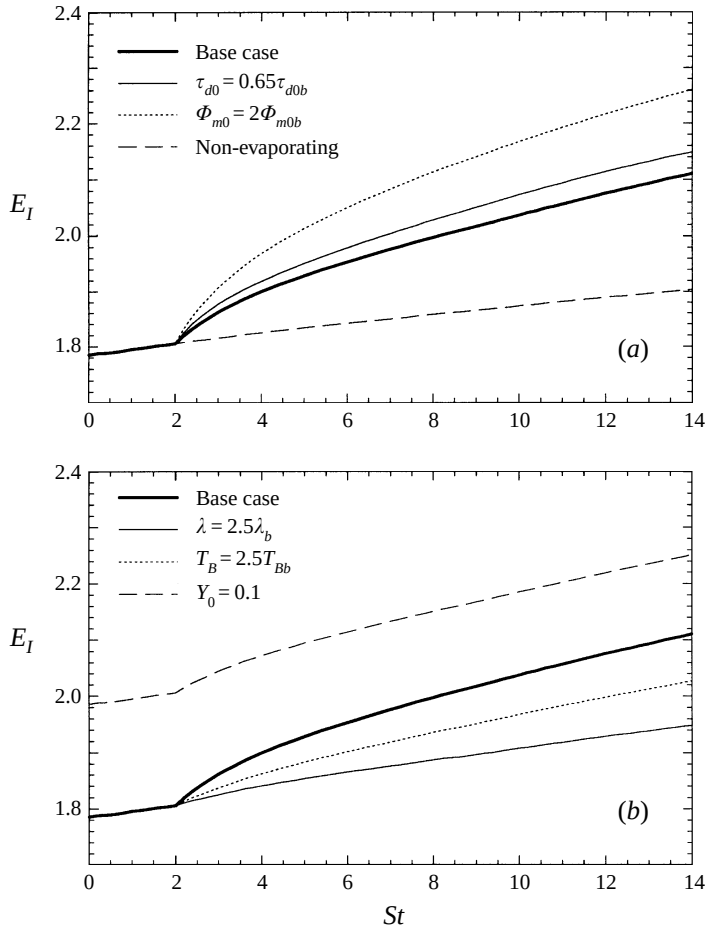

FIGURE 16. Mean internal energy of the carrier phase for evaporating cases.

carrier phase, their temporal variations for all of the cases are considered in figure 18. This figure indicates that, except for a short initial period in the case with $\lambda = 2.5\lambda_b$, H_d is consistently larger than Q_d for all of the cases. Both terms tend to approach asymptotic values at long times with Q_d approaching very small values for most of the cases. The case with $\tau_{d0} = 0.65\tau_{d0b}$ exhibits a sharp decrease in H_d at long times ($St > 12.5$). This is the only case where (within the simulation time) some of the droplets are fully evaporated, resulting in a decrease of the vapour production at long times.

The temporal variations of the mean temperature are shown in figure 19 for both phases. For all of the cases, a sharp decrease in the droplet mean temperature is observed immediately after the evaporation begins. This is due to the initial large difference between the vapour mass fraction at the surface of the droplet (Y_s) and that in the surrounding carrier phase (Y^*). This difference is positive during the early times and, as (7) indicates, tends to decrease the droplet internal energy. The physical interpretation is that initially the droplets are not in equilibrium with the vapour in their surrounding carrier phase, and a large gradient exists for the vapour concentration around each droplet. This causes the droplet to evaporate with a high rate. Since the temperature difference between the two phases is small during this initial

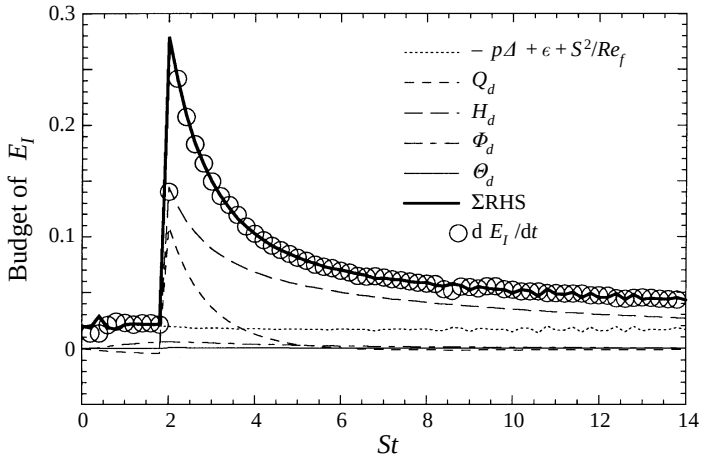

FIGURE 17. Budget of the mean internal energy of the carrier phase for the evaporating case with $\tau_{d0} = 1$ and $\Phi_{m0} = 0.2$.

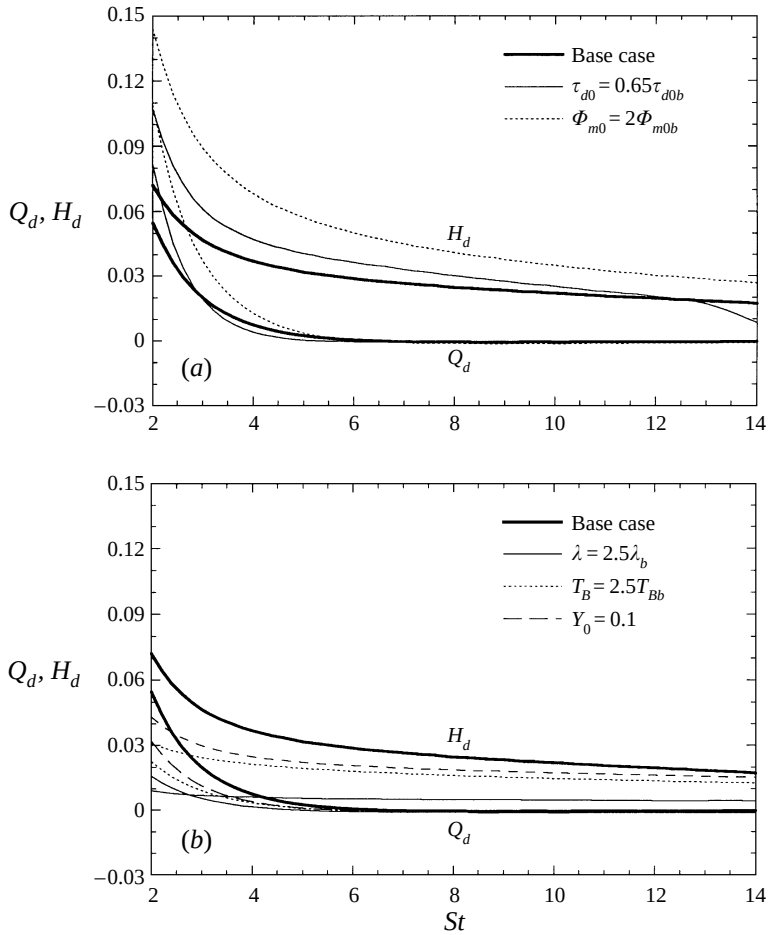

FIGURE 18. Rate of change of the mean internal energy of the carrier phase by Q_d and H_d.

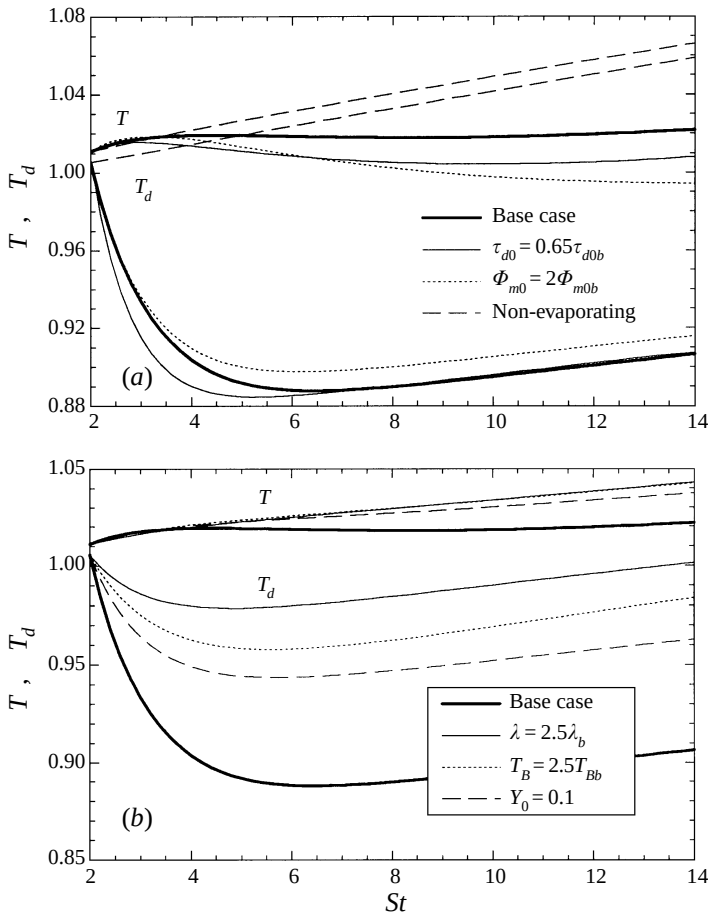

FIGURE 19. Mean temperature of the carrier phase and the droplets for evaporating cases.

period the convective heat transfer from the carrier phase to the droplets is not very effective and the energy required for phase change must be provided by decreasing the internal energy of the droplets. Once the temperature difference is increased the energy required for evaporation can be supplied by heat transfer from the carrier phase. In the meantime, evaporation results in the decrease of the difference between the vapour mass fraction at the surface of the droplet and that in the carrier phase. Thus, at long times the first term in the droplet temperature equation (7) is larger than the second term and the droplet temperature begins to increase. In summary, in the beginning evaporation is mainly due to the vapour concentration gradient while at long times it is supported by heat transfer from the carrier phase. This becomes more clear by considering the ratio of the magnitudes of the convective heat transfer, $f_2(T^* - T_d)/\tau_d$, and the phase change energy, $f_3(Y_s - Y^*)/\tau_d$, in the droplet energy equation (7). An examination of the temporal variation of $\langle\langle f_2(T^* - T_d)\rangle\rangle / \langle\langle f_3(Y_s - Y^*)\rangle\rangle$ indicated that this ratio starts from small values at $St = 2$ and then approaches asymptotic values at long time. Table 3 shows that the asymptotic value is larger than 1 for all of the cases. Therefore, at long times the heat transfer from the carrier phase to the droplets is larger than the amount of heat required for phase change and the droplet temperature increases in time. The largest asymptotic value is obtained in the case

Case	$\dfrac{\langle\langle f_2(T^* - T_d)\rangle\rangle}{\langle\langle f_3(Y_s - Y^*)\rangle\rangle}$
base case	**1.019**
$\tau_{d0} = 0.65\tau_{d0b}$	1.009
$\Phi_{m0} = 2\Phi_{m0b}$	1.029
$\lambda = 2.5\lambda_b$	1.138
$T_B = 2.5T_{Bb}$	1.088
$Y_0 = 0.1$	1.040

TABLE 3. Asymptotic values for the ratio of the convective heat transfer and the heat transfer due to phase change of the droplets.

with the largest latent heat of evaporation. This is due to significant decrease of the evaporation rate in this case.

An inspection of the r.m.s. of the temperature fluctuations (not shown) for both phases indicated that, similarly to non-evaporating cases, the r.m.s.-temperature fluctuation of the carrier phase is larger than that of the droplets for all of the cases. Evaporation results in an increase of T_{rms} while decreasing T_{drms}. Also, T_{rms} is rather insensitive to the droplet time constant or the mass loading ratio while T_{drms} slightly increases with the decrease of the droplet time constant. As expected, the r.m.s. fluctuating temperatures of both phases depend on the variations of the thermodynamic variables: T_{rms} decreases with the increase of λ or T_B while opposite trends are observed for T_{drms}.

5.3. *Evaporation rate*

An important issue in the study of evaporating droplets is the evaporation rate as identified by the rate of change of the mean-squared droplet diameter ($\langle\langle d_d^2\rangle\rangle/d_{d0}^2$). The temporal variations of $\langle\langle d_d^2\rangle\rangle/d_{d0}^2$ are shown in figure 20 for different cases. It is observed that during the early stages of evaporation ($2 < St < 4$) the evaporation rate is nonlinear. This is due to the fact that during this time evaporation is controlled by the vapour concentration gradient as discussed in § 5.2. At long times, the droplets come to an equilibrium with the vapour mass fraction in the surrounding fluid and the rate of evaporation approaches a relatively constant value. Therefore, the long-time evaporation rate is expected to be more in agreement with the classical d^2-law (Williams 1985). The magnitude of the evaporation rate is, however, dependent on different parameters which is discussed below.

Figure 20(a) shows that the decrease of the droplet time constant increases the evaporated mass of the droplets. Equation (8) indicates that the rate of change of d_d^2/d_{d0}^2 is inversely proportional to d_{d0}^2. Therefore, with the increase of τ_d, the evaporation rate decreases and so does the evaporated mass of the droplets. The physical explanation is that smaller droplets have a larger surface to volume ratio than larger droplets. Since the evaporated mass is proportional to the surface area, the smaller droplets evaporate more mass per unit volume. Figure 20(a) also shows that the increase of the mass loading ratio decreases the relative (to initial mass) evaporated mass of the droplets. This is due to the increase of the vapour mass fraction (Y) as the absolute evaporated mass increases with the increase of the mass loading ratio. Consequently, $(Y_s - Y^*)$, which determines the rate of evaporation (see equation (8)), decreases and individual droplets evaporate with smaller rates. The increase of λ can be interpreted as the increase of the droplet latent heat of

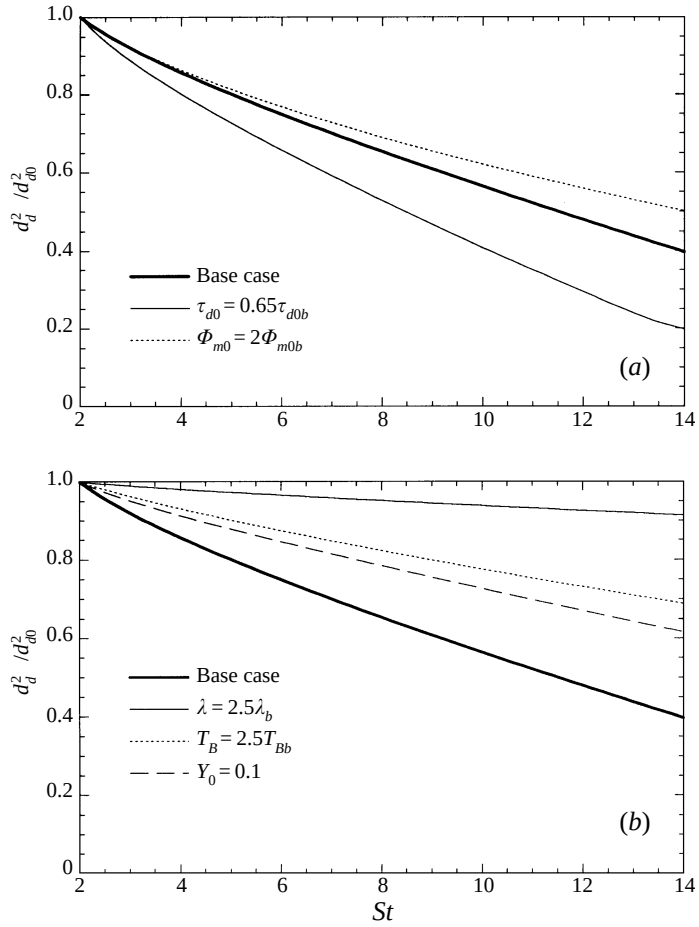

FIGURE 20. Temporal variations of the mean droplet diameter squared normalized with its initial value.

evaporation and, as shown in figure 20(*b*), delays the evaporation process. This is also evident from (13) which indicates a decrease in Y_s, and therefore the evaporation rate, with the increase of λ. The increase of the boiling temperature also decreases Y_s, thus resulting in the decrease of the evaporation rate. Finally, the increase of the initial vapour mass fraction decreases the difference $(Y_s - Y^*)$ and the evaporation rate.

The results presented in figure 20(*a*) suggest that the rate of evaporation is higher for smaller droplets. To provide more evidence for this observation, in figure 21 we consider the joint probability density function (p.d.f.) of the droplet time constant and the evaporation rate for the base case at $St = 12$. Both of these variables are normalized with their respective mean values at $St = 12$. The figure shows that for each droplet time constant there is a range of possible evaporation rates. However, the skewness of the p.d.f. indicates that smaller droplets exhibit higher probabilities of experiencing high evaporation rates than larger droplets do. It is also noted that the highest p.d.f. values belong to droplets of moderate sizes having moderate rates of evaporation.

It is well established that droplets (with moderate sizes) tend to escape from high-vorticity regions and to collect in the regions of the flow with high strain rates (Wang & Maxey 1993; Eaton & Fessler 1994). However, it is not yet clear how the evaporation

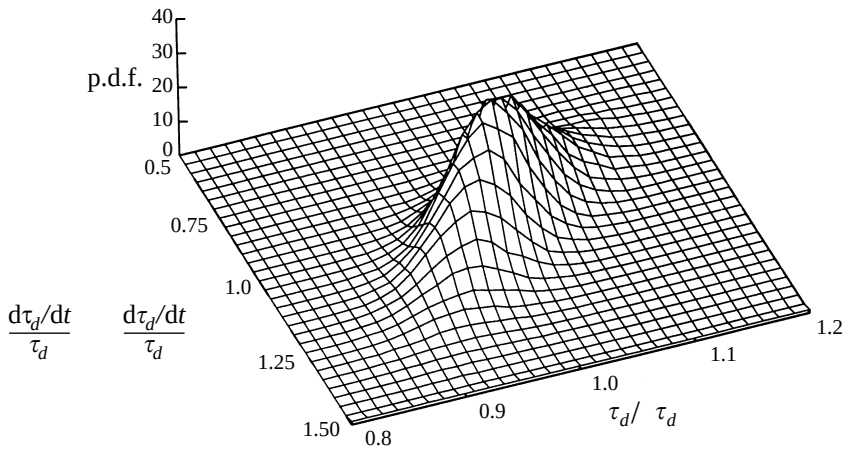

FIGURE 21. Joint p.d.f. of the evaporation rate and the droplet time constant at $St = 12$ for the base case.

rate is affected by the flow structure. Here, the DNS results are utilized to address this issue. A convenient parameter for distinguishing various regions in the flow is

$$II_d \equiv -\tfrac{1}{2}\left(\frac{\partial u_i}{\partial x_j}\frac{\partial u_j}{\partial x_i}\right) = -\tfrac{1}{2}\left(\xi^2 - \tfrac{1}{4}\omega_i\omega_i\right), \tag{42}$$

where ξ^2 denotes the the magnitude of the strain-rate tensor. In incompressible flows, II_d represents the second invariant of the deformation tensor, $\partial u_i/\partial x_j$, (see e.g. Squires & Eaton 1990). For a compressible flow, II_d does not have an analogous physical significance; however, it may still be used for flow characterization as the negative and positive values of II_d correspond to high strain rate and high vorticity regions of the flow, respectively. It must be emphasized that the parameter II_d is defined based on fluctuating velocities, and does not take into account the large-scale motions due to mean shear. Since the droplets have the same mean velocity as that of the carrier phase, they simply follow these large-scale motions, and only turbulent motions contribute to the preferential effects of the flow on the droplets.

Figure 22 shows contours of the joint p.d.f. of the evaporation rate (normalized with its mean value) and II_d (normalized with its r.m.s. value) for the base case and the case with $\tau_{d0} = 0.65\tau_{d0b}$. The p.d.f. is calculated using the interpolated values of II_d at the droplet location. In order to eliminate the effects of the droplet size variations on the evaporation rate, these joint p.d.f.s are calculated at the onset of evaporation ($St = 2$) when the droplets still have identical sizes. In the figure, the joint p.d.f. takes the highest value on the innermost contour and decreases towards the outermost contour. Figure 22 clearly shows that, for both cases, the p.d.f.s are skewed such that the probability of finding higher evaporation rates is larger in the high strain rate (negative II_d) regions of the flow than in the high vorticity (positive II_d) regions. Therefore, not only do the droplets tend to collect in the high strain rate regions of the flow, they also exhibit higher evaporation rates in these regions. As a result, the overall effect is to expedite the evaporation process.

To further elaborate on this issue, we assess the effects of the parameters that directly influence the evaporation rate. By manipulating (8), it is easy to show that $\mathrm{d}\tau_d/\mathrm{d}t \propto \rho^*(2 + 0.6Re_d^{0.5}Sc^{0.33})(Y_s - Y^*)$. At $St = 2$, Y^* is the same for all of the droplets, thus, the evaporation rate depends on Re_d, Y_s, and ρ_d, where Y_s is a function

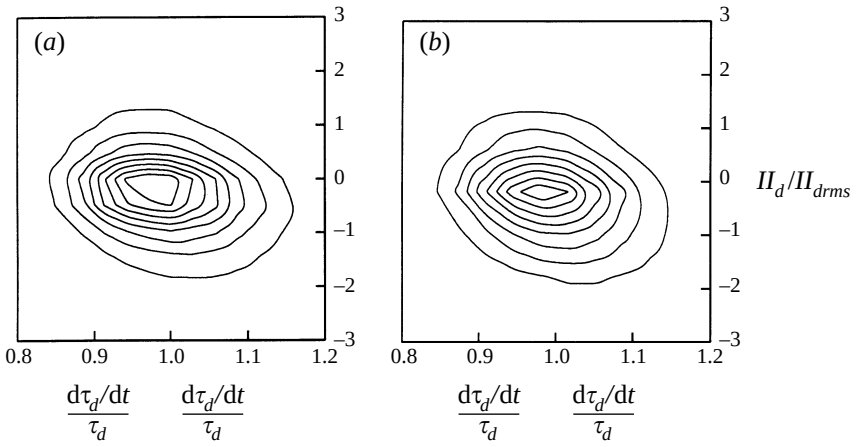

FIGURE 22. Contours of the joint p.d.f. of II_d and the evaporation rate at $St = 2$. (*a*) The base case; contour levels from 0.194 to 2.911 with increment of 0.388. (*b*) The case with $\tau_{d0} = 0.65\tau_{d0b}$; contour levels from 0.2048 to 3.0722 with increment of 0.4096. The highest value belongs to the innermost contour.

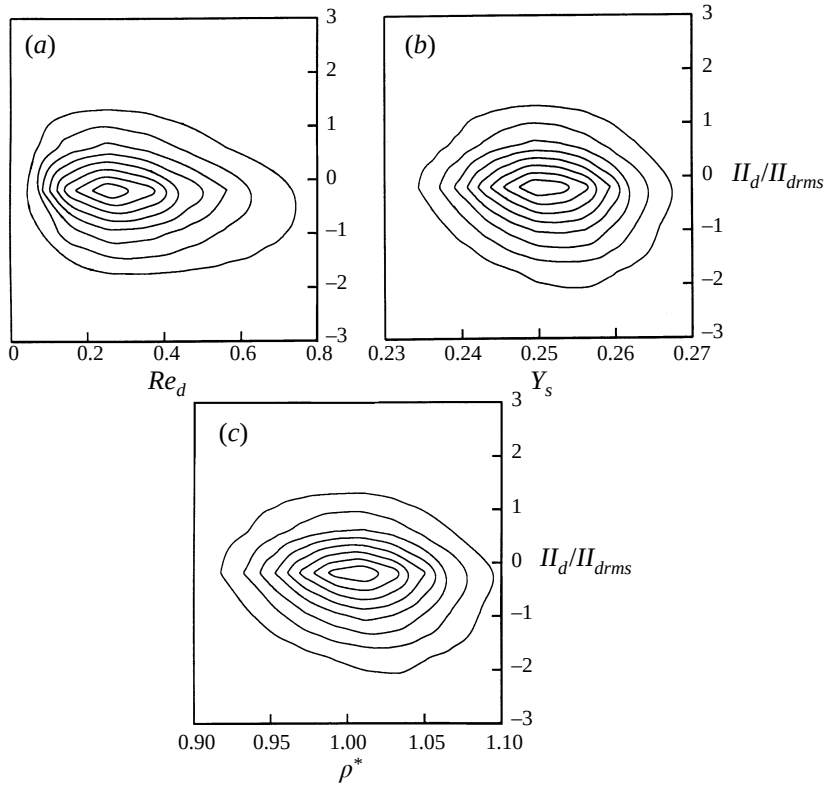

FIGURE 23. Contours of the joint p.d.f. of II_d and (*a*) the droplet Reynolds number; contour levels from 0.0873 to 1.3097 with increment of 0.1746, (*b*) the vapour mass fraction on the droplet surface; contour levels from 1.813 to 27.195 with increment of 3.626, and (*c*) the carrier-phase density at the droplet location; contour levels from 0.3254 to 4.8818 with increment of 0.6509, for the case with $\tau_{d0} = 0.65\tau_{d0b}$ at $St = 2$. The highest value belongs to the innermost contour.

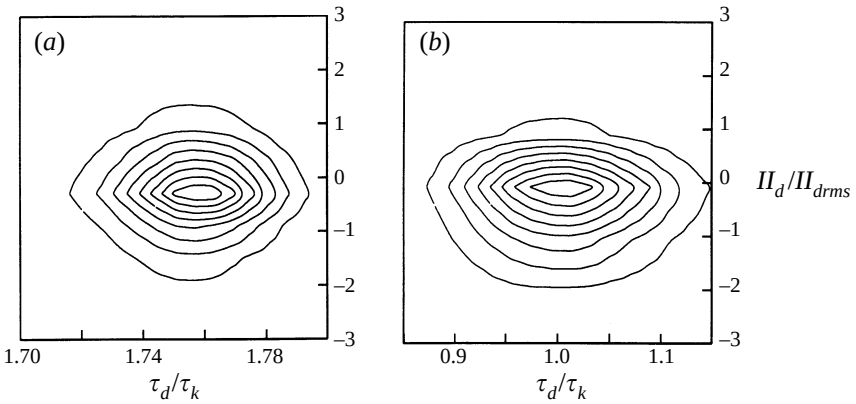

FIGURE 24. Contours of the joint p.d.f. of II_d and the droplet time constant for the case with $\Phi_{m0} = 2\Phi_{m0b}$ at (*a*) $St = 4$; contour levels from 0.8468 to 12.701 with increment of 1.6935, and (*b*) $St = 14$; contour levels from 0.2273 to 3.4088 with increment of 0.4545. The highest value belongs to the innermost contour.

of the droplet temperature and increases with the increase of this parameter. Figure 23 shows contours of the joint p.d.f.s of each of these parameters and II_d, for the case with $\tau_{d0} = 0.65\tau_{d0b}$; other cases indicated similar trends. The figure shows that the joint p.d.f.s are skewed towards the high strain rate regions of the flow for larger values of each of these parameters. However, the largest skewness is observed for the droplet Reynolds number which is more directly influenced by the velocity field. This suggests that a similar phenomenon should be observed for incompressible flows with either one- or two-way coupling with droplets.

To investigate the effects of the flow structure on the distribution of vaporizing droplets, in figure 24 contours of the joint p.d.f. of II_d and the droplet time constant are considered at $St = 4$ and $St = 14$ for the case with $\Phi_{m0} = 2\Phi_{m0b}$. The droplet time constant is normalized with the Kolmogorov time scale since the ratio of the two is the most appropriate parameter to characterize the effects of the preferential distributions. In turbulent flows generated via DNS, the largest effect of preferential distribution is observed for droplet time constants of the order of the Kolmogorov time scale (Wang & Maxey 1993). Figure 24 shows that, at any droplet time constant, there is a higher probability of finding droplets in the high strain rate regions than there is in the high vorticity regions of the flow. However, there is no definite indication that any particular size of the droplets is more influenced by preferential distribution effects than other sizes are. This is probably due to the small range of size variation within each group of droplets. Nevertheless, a comparison of figures 24(*a*) and 24(*b*) indicates that as the average droplet time constant becomes closer to the Kolmogorov time scale, the probability of finding droplets in high vorticity regions of the flow decreases. This is in agreement with previous observations for solid particles.

5.4. *Effects of the initial droplet temperature*

Thus far in this section we have discussed evaporation characteristics when initially the droplets have the same temperature as that of the carrier phase. With this initial condition imposed for the droplet temperature, the early stages of evaporation are mainly controlled by the vapour concentration gradient around the droplet. In practice, however, there are situations where the temperature difference between the two phases is not negligible. It is expected that in these situations the evaporation

τ_{d0}	Φ_{m0}	λ	T_B	Y_0	T_{d0}	Evaporation
1	**0.1**	**0.8**	**2**	**0**	**0.2**	**Yes**
1	0.1	2	2	0	0.2	Yes
1	0.1	0.8	5	0	0.2	Yes

TABLE 4. Cases considered to study the effects of the initial droplet temperature. The base case is shown by boldface.

process is more strongly dictated by the convective heat transfer between the phases rather than by the vapour concentration gradient. In order to address this issue, in this subsection we consider three cases with initial droplet temperature of $T_{d0} = 0.2$. Another important issue to be addressed by this study is whether or not the effects of the initial droplet temperature on the statistics vanish at long times. Table 4 provides a listing of cases considered in this subsection. Notice that these cases are similar to cases considered in table 2, and the only difference is in the magnitude of the initial droplet temperature. For these cases also evaporation starts at $St = 2$.

Figure 25 shows the temporal variations of the mean and the r.m.s. fluctuating temperature for both phases. During the pre-evaporation period ($St < 2$) the mean droplet temperature significantly increases as a result of the convective heat transfer from the carrier phase; at the onset of evaporation ($St = 2$) the mean temperature difference $\langle\langle T^* - T_d \rangle\rangle = 0.235$ for all of the cases. After evaporation begins, figure 25(a) indicates that the increase of either λ or T_B increases the mean temperature of both phases. This is in agreement with the trends observed in figure 19 for cases with $T_{d0} = 1$. Figure 25(b) shows that at long times, both T_{rms} and T_{drms} approach stationary values. A comparison of these results with those for cases with $T_{d0} = 1$ revealed that the asymptotic values are very close. This suggests that the effects of the initial droplet temperature on long-time values of both T_{rms} and T_{drms} are rather insignificant.

In figure 26 we show the variations of the rate of change of the droplet diameter squared, which is an indication of the evaporation rate, for both $T_{d0} = 0.2$ and $T_{d0} = 1$. As expected, during the early stages of evaporation, the evaporation rate is greatly influenced by the decrease of T_{d0}. At long times, the evaporation rate approaches asymptotic values for both of the initial droplet temperatures. However, the asymptotic values in cases with $T_{d0} = 0.2$ are smaller than those in cases with $T_{d0} = 1$. The lower evaporation rates for cases with small initial droplet time constant are attributed to the smaller mean droplet temperature. This decreases the vapour mass fraction on the surface of the droplet which, in turn, results in the decrease of the evaporation rate as indicated by (8).

More insight into the evaporation mechanism is gained by examining the quantity $\langle\langle f_2(T^* - T_d)\rangle\rangle / \langle\langle f_3(Y_s - Y^*)\rangle\rangle$. As was mentioned earlier in § 5.2, this quantity represents the ratio of the convective heat transfer and the phase change energy in the droplet energy equation. The temporal variations of this ratio are shown in figure 27 for both small and large initial values of the droplet temperature. It is observed that in cases with small initial droplet temperature $\langle\langle f_2(T^* - T_d)\rangle\rangle / \langle\langle f_3(Y_s - Y^*)\rangle\rangle$ starts from large values. This is expected as when the initial droplet temperature is low the convective heat transfer is dominant. It is also due to small values of Y_s which decreases the evaporation rate and, consequently, the phase change energy. In general, figure 27 shows that the early stages of evaporation are dominated by convective heat transfer

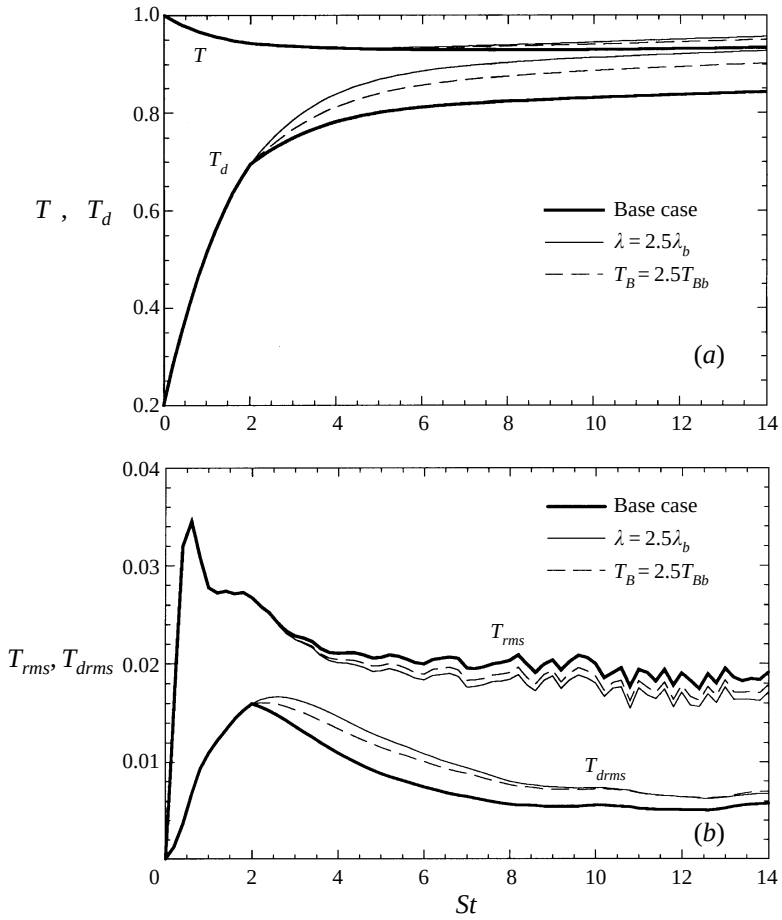

FIGURE 25. Temporal variations of (*a*) the mean and (*b*) the fluctuating temperature of the carrier phase and the droplets for evaporating cases with $T_{d0} = 0.2$.

in the case with small initial droplet temperature, whereas in the case with large initial droplet temperature the phase change mechanism is more effective. At long times, all of the cases approach asymptotic values which are somewhat dependent on the initial droplet temperature.

The variations of the droplet temperature significantly affects the vapour mass fraction on the surface of the droplet (Y_s) as well as the carrier-phase density at the droplet location (ρ^*). Therefore, it may be expected that the decrease of the initial droplet temperature should have a significant influence on the variation of the evaporation rate in various regions of the flow. However, contours of the joint p.d.f. of the normalized evaporation rate and II_d (shown in figure 28 for the base case at $St = 2$) suggest that this is not the case. In fact, comparisons of the joint p.d.f.s of Re_d, Y_s, or ρ_d, and II_d indicated that in this case also the droplet Reynolds number has the largest effect on the variations of the evaporation rate. This, again, suggests that the velocity field is more influential in preferential variations of the evaporation rate than are the thermodynamic fields.

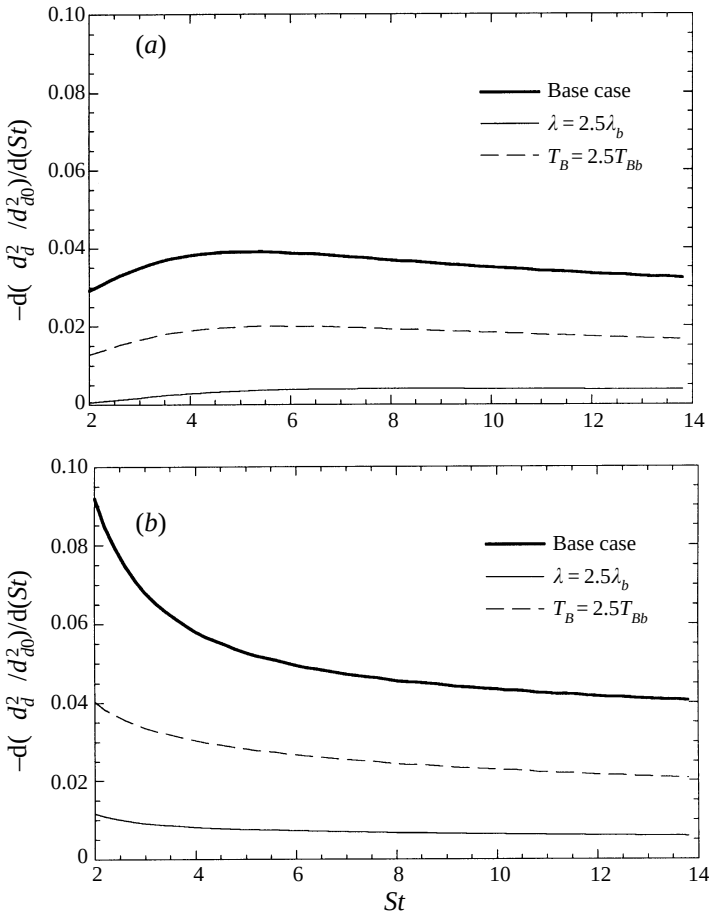

FIGURE 26. The rate of change of the mean droplet diameter squared. (*a*) $T_{d0} = 0.2$, (*b*) $T_{d0} = 1$.

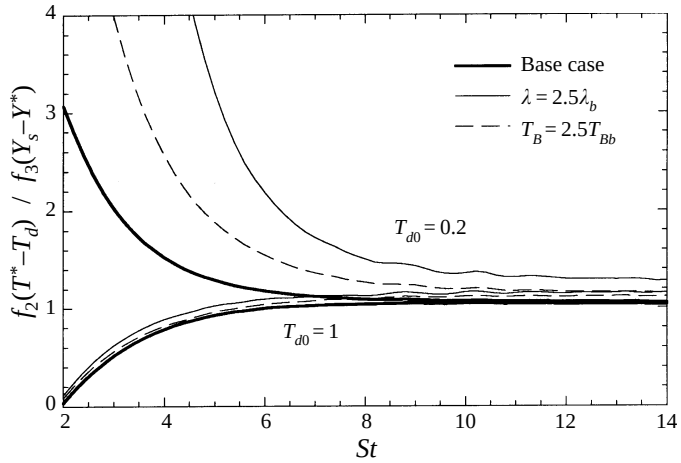

FIGURE 27. Ratio of the convective heat transfer to the energy transfer by phase change in the droplet energy equation.

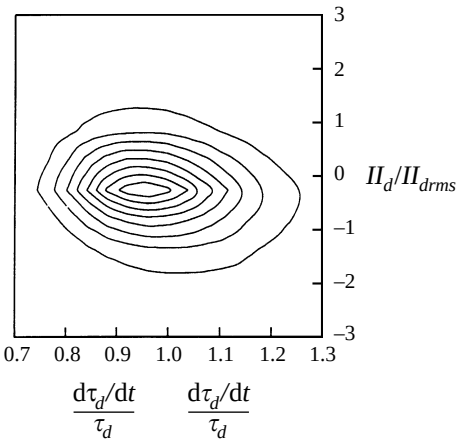

FIGURE 28. Contours of the joint p.d.f. of II_d and the evaporation rate at $St = 2$ for the base case with $T_{d0} = 0.2$; contour levels from 0.1281 to 1.9223 with increment of 0.2563. The highest value belongs to the innermost contour.

6. Summary and concluding remarks

An extensive DNS study is carried out of the dispersion and polydispersity of droplets in low-Mach-number homogeneous turbulent shear flows. A study of large compressibility effects is not intended, and the mean turbulent Mach number is less than 0.2. The effects of density variations, however, are fully considered by solving the equations of the compressible flow. Cases with one- and two-way coupling are considered for either non-evaporating or evaporating droplets. The formulation presented in § 2 includes all modes of mass, momentum, and energy transfer between the two phases (in the limit of small volume fractions) – radiation heat transfer is neglected. The gravity effects are not considered as the numerical methodology is only applicable in the absence of gravity. The carrier phase (composed of the gas and the vapour) is described in the Eulerian frame and the droplets are tracked in a Lagrangian manner.

In the study of non-evaporating droplets, the effects of the droplet time constant, the mass loading ratio, the droplet specific heat, and the initial droplet temperature on the velocity and thermodynamic fields are examined. The kinetic energy of the carrier phase decreases with the increase of the mass loading ratio, or the increase of the droplet time constant. It also decreases with the decrease of the droplet initial temperature but is insensitive to the variations of the droplet specific heat. These trends are explained by considering the budget of the carrier-phase turbulence kinetic energy. The pressure–dilatation correlation contributes most to the decrease of the kinetic energy with the decrease of the initial droplet temperature. The droplet time constant and the mass loading ratio are shown to influence the carrier-phase kinetic energy mostly through drag. The droplet streamwise velocity variance is larger than the fluid one and the ratio of the two increases with the increase of the droplet time constant. This is in agreement with recent theories in homogeneous shear flows; however, it is the opposite of the trends observed in isotropic flows. An examination of the budget of the droplet streamwise velocity variance indicates that the production by the mean droplet velocity gradient is responsible for this phenomenon.

The budget of the mean internal energy of the carrier phase is also carefully examined in order to assess various mechanisms for the exchange of the internal energy between the phases. As expected, the mean internal energy has the largest

variations when the initial droplet temperature is decreased. This is due to the increase of the convective heat transfer from the carrier phase to the droplets. For cases in which the droplets initially have the same temperature as that of the carrier phase, the internal energy generated due to the dissipation of the kinetic energy by drag (Φ_d) is of the same order of importance as the convective heat transfer. The mean temperature difference between the phases and the r.m.s. of the fluctuating temperatures of both phases approach asymptotic values at long times. These asymptotic values seem to be independent of the initial droplet temperature.

A similar study is conducted for the evaporating droplets in which the effects of the initial droplet time constant, the initial mass loading ratio, the droplet latent heat of evaporation, the boiling temperature, the initial vapour mass fraction, and the initial droplet temperature are considered. The trends observed for the variations of the turbulence kinetic energy of the carrier phase are different than those in the non-evaporating cases. This is mainly due to the kinetic energy carried to the carrier phase by the vapour. An examination of the budget of the turbulence kinetic energy has revealed that this energy transfer is of the same order of importance as the energy exchange by drag. It is also shown that evaporation decreases the level of anisotropy of the flow that is caused by the droplets.

The mean internal energy of the carrier phase is significantly increased by evaporation. This is again due to the transfer of energy from the droplets to the carrier phase by the vapour. This effect is more visible for the mean internal energy than it is for the turbulence kinetic energy as (for the parameter ranges considered here) the specific internal energy of the vapour is always larger than that of the gas at the same temperature. The variations of the mean temperatures of both phases are explained by discussing the evaporation mechanism. It is shown that, when the initial temperature difference between the phases is negligible, the evaporation is controlled by the vapour concentration gradient around the droplets. This results in a sharp decrease of the mean temperature of the droplets during the early times. When the initial droplet temperature is significantly lower than that of the carrier phase, evaporation is mostly dictated by convective heat transfer. The decrease of the initial droplet temperature also has a major impact on the evaporation rate during the early times. The small values of the droplet temperature decrease the vapour mass fraction on the surface of the droplet and result in substantial decrease of the evaporation rate. The long-time values of the evaporation rate, however, show smaller sensitivity to the initial droplet temperature. An examination of the r.m.s. of the temperature fluctuations of the carrier phase and the droplets for evaporating cases with different initial droplet temperatures indicates that the long-time values of this parameter become independent of the initial conditions.

The effects of the flow structure on the dispersion of the droplets and the evaporation rate are studied by considering the joint p.d.f.s of various parameters. The smaller droplets experience higher evaporation rates, mainly due to larger surface area to volume ratios. It is shown that the droplets residing in high strain rate regions of the flow exhibit higher evaporation rates. A study of the parameters influencing the evaporation rate indicates that the droplet Reynolds number is the most influential parameter for this preferential behaviour. Similarly to previous findings in the dispersion of solid particles, it is observed that evaporating droplets tend to preferentially collect in high strain rate regions of the flow. Therefore, the overall effect of the flow structure is to expedite the evaporation process.

This DNS study aids to improve our state of knowledge on interactions between the droplets and turbulence in homogeneous shear flows. One may also be interested

in using the data generated by these direct simulations to validate turbulence models developed for two-phase flows. While this approach has been successfully adopted in incompressible flows (Mashayek, Taulbee & Givi 1997*b*; Mashayek, Taulbee & Givi 1998*a*, *b*), it must be mentioned that certain limitations apply to the current compressible flow results. These are mainly due to the small Reynolds numbers produced in these simulations. The study by Blaisdell *et al.* (1991) has shown that, even in compressible flows at higher Reynolds numbers than those considered here, the available turbulence models (for single-phase flows) perform unsatisfactorily. In particular, the pressure–strain correlation models and the assumption of isotropic dissipation, which are the cornerstones of any statistical turbulence modelling, do not seem to comply with the results of these simulations. Therefore, before any attempt is made to test the two-phase flow models, one has to make sure that the single-phase flow is modelled with reasonable accuracy.

Computational resources for this work were in part provided by the Pittsburgh Supercomputing Center and the College of Engineering Computer Facility at the University of Hawaii at Manoa.

REFERENCES

Balachandar, B. & Maxey, M. R. 1989 Methods for evluating fluid velocities in spectral simulations of turbulence. *J. Comput. Phys.* **83**, 96–125.

Bird, R. B., Stewart, W. E. & Lightfoot, E. N. 1960 *Transport Phenomena.* Wiley.

Blaisdell, G. A., Mansour, N. N. & Reynolds, W. C. 1991 Numerical simulation of compressible homogeneous turbulence. *Department of Mechanical Engineering Rep.* TF-50. Stanford University, Stanford, CA.

Blaisdell, G. A., Mansour, N. N. & Reynolds, W. C. 1993 Compressibility effects on the growth and structure of homogeneous turbulent shear flow. *J. Fluid Mech.* **256**, 443–485.

Corrsin, S. 1961 Turbulent flow. *Am. Scientist* **49**, 300–324.

Crowe, C. T., Sharma, M. P. & Stock, D. E. 1977 The Particle-Source in cell (PSI-Cell) model for gas-droplet flows. *Trans. ASME* I: *J. Fluids Engng* **6**, 325–332.

Eaton, J. K. & Fessler, J. R. 1994 Preferential concentration of particles by turbulence. *Intl J. Multiphase Flow Suppl.* **20**, 169–209.

Elghobashi, S. & Truesdell, G. C. 1992 Direct simulation of particle dispersion in a decaying isotropic turbulence. *J. Fluid Mech.* **242**, 655–700.

Elghobashi, S. & Truesdell, G. C. 1993 On the two-way interaction between homogeneous turbulence and dispersed solid particles. I: Turbulence modification. *Phys. Fluids* **5**, 1790–1801.

Faeth, G. M. 1983 Evaporation and combustion in sprays. *Prog. Energy Combust. Sci.* **19**, 1–76.

Faeth, G. M. 1987 Mixing, transport and combustion in sprays. *Prog. Energy Combust. Sci.* **13**, 293–345.

Givi, P. & Madnia, C. K. 1993 Spectral methods in combustion. In *Numerical Modeling in Combustion* (ed. T. J. Chung), chap. 8, pp. 409–452. Taylor & Francis.

Hinze, J. O. 1972 Turbulent fluid and particle interaction. In *Progress in Heat and Mass Transfer* (ed. G. Hetsroni), vol. 6, pp. 433–452. Pergamon.

Jackson, R. & Davidson, B. J. 1983 An equation set for non-equilibrium two phase flow, and an analysis of some aspects of choking, acoustic propagation, and losses in low pressure wet steam. *Intl J. Multiphase Flow* **9**, 491–510.

Kida, S. & Orszag, S. A. 1990 Energy and spectral dynamics in forced compressible turbulence. *J. Sci. Comput.* **5**, 85–125.

Kida, S. & Orszag, S. A. 1992 Energy and spectral dynamics in decaying compressible turbulence. *J. Sci. Comput.* **7**, 1–34.

Lee, S., Lele, S. K. & Moin, P. 1991 Eddy shocklets in decaying compressible turbulence. *Phys. Fluids* A **3**, 657–664.

Liljegren, L. M. 1993 The effect of a mean fluid velocity gradient on the streamwise velocity variance of a particle suspended in a turbulent flow. *Intl J. Multiphase Flow* **19**, 471–484.

Mashayek, F. 1998 Direct numerical simulations of evaporating droplet dispersion in forced low Mach number turbulence. *Intl J. Heat Mass Transfer* (in press).

Mashayek, F., Jaberi, F. A., Miller, R. S. & Givi, P. 1997*a* Dispersion and polydispersity of droplets in stationary isotropic turbulence. *Intl J. Multiphase Flow* **23**, 337–355.

Mashayek, F., Taulbee, D. B. & Givi, P. 1997*b* Modeling and simulation of two-phase turbulent flow. In *Propulsion Combustion* (ed. G. D. Roy), chap. 8, pp. 241–280. Taylor & Francis.

Mashayek, F., Taulbee, D. B. & Givi, P. 1998*a* Particle-laden turbulent flows. Part 1. Direct simulations and Reynolds stress closures. *J. Fluid Mech.* (submitted).

Mashayek, F., Taulbee, D. B. & Givi, P. 1998*b* Particle-laden turbulent flows. Part 2. Explicit algebraic closures. *J. Fluid Mech.* (submitted).

McLaughlin, J. B. 1989 Aerosol particle deposition in numerically simulated channel flow. *Phys. Fluids* A **1**, 1211–1224.

Miura, H. & Kida, S. 1995 Acoustic energy exchange in compressible turbulence. *Phys. Fluids* A **7**, 1732–1742.

Panton, R. L. 1984 *Incompressible Flow*. John Wiley & Sons.

Passot, T. & Pouquet, A. 1987 Numerical simulation of compressible homogeneous flows in the turbulent regime. *J. Fluid Mech.* **181**, 441–466.

Reeks, W. M. 1993 On the constitutive relations for dispersed particles in nonuniform flows. I: Dispersion in a simple shear flow. *Phys. Fluids* A **5**, 750–761.

Riley, J. J. & Patterson, G. S. 1974 Diffusion experiments with numerically integrated isotropic turbulence. *Phys. Fluids* **17**, 292–297.

Rogallo, R. S. 1981 Numerical experiments in homogeneous turbulence. *NASA Tech. Mem.* 81315.

Rubesin, M. W. 1976 A one-equation model of turbulence of use with the compressible navier-stokes equations. *NASA Tech. Mem.* X-73, 128.

Samimy, M. & Lele, S. K. 1991 Motion of particles with inertia in a compressible free shear layer. *Phys. Fluids* A **3**, 1915–1923.

Sarkar, S. 1992 The pressure-dilatation correlation in compressible flows. *Phys. Fluids* **4**, 2674–2682.

Sarkar, S. 1994 The stabilizing effect of compressibility in turbulent shear flow. *ICASE Rep.* 94-46. NASA Langley Research Center, Hampton, VA.

Sarkar, S., Erlebacher, G. & Hussaini, M. Y. 1991 Direct simulation of compressible turbulence in a shear flow. *ICASE Rep.* 91-29. NASA Langley Research Center, Hampton, VA.

Sarkar, S., Erlebacher, G. & Hussaini, M. Y. 1992 Compressible homogeneous shear: Simulation and modeling. *ICASE Rep.* 92-6. NASA Langley Research Center, Hampton, VA.

Simonin, O., Deutsch, E. & Boivin, M. 1995 Large eddy simulation and second-moment closure model of particle fluctuating motion in two-phase turbulent shear flows. In *Turbulent Shear Flows 9* (ed. F. Durst, N. Kasagi, B. E. Launder, F. W. Schmidt & J. H. Whitelaw), pp. 85–115. Springer.

Squires, K. D. & Eaton, J. K. 1990 Particle response and turbulence modification in isotropic turbulence. *Phys. Fluids* A **2**, 1191–1203.

Squires, K. D. & Eaton, J. K. 1991*a* Measurements of particle dispersion obtained from direct numerical simulations of isotropic turbulence. *J. Fluid Mech.* **226**, 1–35.

Squires, K. D. & Eaton, J. K. 1991*b* Preferential concentration of particles by turbulence. *Phys. Fluids* A **3**, 1169–1178.

Squires, K. D. & Eaton, J. K. 1994 Effect of selective modification of turbulence on two-equation models for particle-laden turbulent flows. *Trans. ASME* I: *J. Fluids Engng* **116**, 778–784.

Taylor, G. I. 1921 Diffusion by continuous movements. *Proc. Lond. Math. Soc.* (2) **20**, 196–211.

Truesdell, G. C. & Elghobashi, S. 1994 On the two-way interaction between homogeneous turbulence and dispersed solid particles. II: Particle dispersion. *Phys. Fluids* **6**, 1790–1801.

Wallis, G. B. 1969 *One Dimensional Two Phase Flow*. McGraw Hill.

Wang, L-P. & Maxey, M. R. 1993 Settling velocity and concentration distribution of heavy particles in isotropic turbulence. *J. Fluid Mech.* **256**, 27–68.

Williams, F. A. 1985 *Combustion Theory*, 2nd Edn. Benjamin/Cummings.

Yeung, P. K. & Pope, S. B. 1988 An algorithm for tracking fluid particles in numerical simulations of homogeneous turbulence. *J. Comput Phys.* **79**, 373–416.